**Title: Immune Signatures of SARS-CoV-2 Infection Resolution in Human Lung Tissues**

**Short Title: SARS-CoV-2 infection resolution in human lung tissues**

**One sentence summary:** We comprehensively mapped the human immunological dynamics associated with successful resolution of SARS-CoV-2 infection in human lung tissues.

Devin Kenney[1,2], Aoife K. O'Connell[1,2,4], Anna E. Tseng[1,2,4], Jacquelyn Turcinovic[1,2,3], Maegan L. Sheehan[7,12], Adam D. Nitido[7,12], Paige Montanaro[2,4], Hans P. Gertje[2,4], Maria Ericsson[6], John H. Connor[1,2], Vladimir Vrbanac[7], Nicholas A. Crossland[1,2,4], Christelle Harly[8,9,12]*, Alejandro B. Balazs[7,12]*, and Florian Douam[1,2,12,13] *

[1]Department of Virology, Immunology, and Microbiology, Boston University Chobanian & Avedisian School of Medicine, Boston, MA, USA.

[2] National Emerging Infectious Diseases Laboratories, Boston University, Boston, MA, USA.

[3] Bioinformatics Program, Boston University, Boston, MA, USA.

[4] Department of Pathology and Laboratory Medicine, Boston University Chobanian & Avedisian School of Medicine, Boston, MA, USA.

[6] Electron Microscopy Core Facility, Harvard Medical School, Boston, MA, USA.

[7] Ragon Institute of MGH, MIT and Harvard, Cambridge, MA, USA.

[8] Université de Nantes, INSERM, CNRS, CRCINA, Nantes, France

[9] LabEx IGO 'Immunotherapy, Graft, Oncology', Nantes, France.

[12] These authors contributed equally to the work.

[13] Lead contact

*Correspondence:

Florian Douam, National Emerging Infectious Diseases Laboratories, 620 Albany Street Boston MA 02118 USA, +1-617-358-9174, fdouam@bu.edu.

Alejandro B. Balazs, Ragon Institute of MGH Harvard and MIT, 400 Technology Square Cambridge MA 02139 USA, +1-857-268-7197, abalazs@mgh.harvard.edu.

Christelle Harly, CRCINA - Institut de Recherche en Santé de Nantes Université, 8 quai Moncousu 44 007 Nantes France, +33-2 28 08 02 08, christelle.harly@inserm.fr.

The authors have declared that no conflict of interest exists.

**ABSTRACT**

While human autopsy samples have provided insights into pulmonary immune mechanisms associated with severe viral respiratory diseases, the mechanisms that contribute to a clinically favorable resolution of viral respiratory infections remain unclear due to the lack of proper experimental systems. Using mice co-engrafted with a genetically matched human immune system and fetal lung xenograft (fLX), we mapped the immunological events defining successful resolution of SARS-CoV-2 infection in human lung tissues. Viral infection is rapidly cleared from fLX following a peak of viral replication, histopathological manifestations of lung disease and loss of AT2 program, as reported in human COVID-19 patients. Infection resolution is associated with the activation of a limited number of hematopoietic subsets, including inflammatory monocytes and non-canonical double-negative T-cells with cytotoxic functions, which are highly enriched in viral RNA and dissipate upon infection resolution. Activation of specific human fibroblast and endothelial subsets also elicit robust antiviral and monocyte chemotaxis signatures, respectively. Notably, systemic depletion of human CD4+ cells, but not CD3+ cells, abrogates infection resolution in fLX and induces persistent infection, supporting evidence that peripheral CD4+ monocytes are important contributors to SARS-CoV-2 infection resolution in lung tissues. Collectively, our findings unravel a comprehensive picture of the immunological events defining effective resolution of SARS-CoV-2 infection in human lung tissues, revealing markedly divergent immunological trajectories between resolving and fatal COVID-19 cases.

## INTRODUCTION

Coronavirus disease 2019 (COVID-19) is a respiratory disease that has swept the world since its emergence in the Wuhan province of China in late 2019. The etiologic agent of COVID-19, the Severe Acute Respiratory Syndrome Coronavirus 2 (SARS-CoV-2) is a plus-sense, enveloped RNA virus that targets the epithelium of the respiratory tract. Infection results in varying severities of COVID-19, with most cases being mild to asymptomatic. The onset of severe disease is associated with aberrant immune responses (e.g., excessive pulmonary infiltration of myeloid cells, inflammasome-activated monocytic cells, macrophage exacerbated inflammation) and severe lung injury (e.g., lung consolidation, diffuse alveolar damage (DAD), and thrombosis) (*1-9*).

A large number of human studies have been instrumental in unraveling cellular and molecular processes driving severe COVID-19 disease in infected tissues, particularly in the respiratory tract, using autopsy samples (*10-13*). In parallel, human studies of resolving COVID-19, including controlled human challenge studies, have leveraged peripheral blood and nasopharyngeal samples to identify human signatures of effective infection resolution and mild disease (*14-16*). Notably, this includes individuals with specific HLA haplotypes (*15*), evidence of previous coronavirus exposure (*15, 17, 18*), rapid nasopharyngeal immune infiltration (*14*), and non-productive infection of nasopharyngeal T-cells and macrophages (*14*). However, tissue-specific human immunological processes associated with protection, such as extravasation of recruited immune lineages and their differentiation processes, have remained elusive due to the ethical considerations associated with tissue sampling of individuals with mild disease and human challenge models. Although large and small animal models of COVID-19 are available, the high-cost and limited reagent availability associated with non-human primate models, and the large divergence between rodent and human immune systems (*19, 20*) further underscore the need for additional models capable of recapitulating human protective immune responses to SARS-CoV-2 infection.

104 Mice engrafted with human fetal lung xenograft (fLX) support infection by multiple human
105 respiratory viruses, including human cytomegalovirus (HCMV), Middle East respiratory syndrome
106 coronavirus (MERS-CoV) and SARS-CoV-2 (*21-23*). Upon co-engraftment with a human immune
107 system (HIS), these animals also mount lung-resident human immune responses against these
108 pathogens (*21, 23-25*). Recently, our group reported that mice engrafted with fLX are highly
109 susceptible to SARS-CoV-2 infection and lung tissue damage and support persistent viral
110 infection (*23*). However, co-engraftment of fLX and HIS in a xenorecipient strain supporting
111 enhanced myelopoiesis (i.e., HNFL mouse model) rapidly blunted viral infection and prevented
112 widespread acute viral replication across fLX, resulting in protection from histopathology of fLX
113 (*23*). Our findings unraveled a human macrophage antiviral signature as a correlate of such rapid
114 protection against SARS-CoV-2 infection. However, how the human immune system mobilizes
115 and resolves infection upon extensive viral replication within human lung tissues, a context that
116 more likely describes mild cases of SARS-CoV-2 infection, has remained elusive.

117 In this study, we leverage previously described immunodeficient mice engrafted with a
118 human fetal lung xenograft (fLX) and a genetically matched human immune system, fetal liver
119 and thymus (BLT-L mice) (*21*) to conduct the first comprehensive mapping of human
120 immunological correlates of resolution of acute SARS-CoV-2 infection in human lung tissues.
121 Consistent with previous reports (*24, 25*), BLT-L mice are permissive to SARS-CoV-2 infection
122 following direct viral inoculation into the fLX. Infection swiftly resolves by 6 days post-infection
123 (dpi) following an early viral replication peak at 2 dpi. Acute viral infection is associated with lung
124 histopathological damage and loss of AT2 program, as described in COVID-19 patients (*1*).
125 Notably, acute infection is also defined by the emergence of a limited set of hyper-activated
126 hematopoietic subsets, including inflammatory monocytes and T-cells expressing genes
127 canonically found in macrophages. Of these, inflammatory monocytes appear to mount the most
128 robust antiviral responses and are highly enriched in viral RNA before phasing out from the tissues
129 after resolution. No inflammasome activation in these cells was observed despite enrichment in

130 viral RNA. This contrasts with reports from fatal COVID-19 cases (*26*) and evidence suggesting
131 that monocyte and macrophage infections in vitro and in vivo are associated with inflammasome
132 activation (*27, 28*).

133 Specific fibroblast and endothelial cell subsets also contribute to antiviral responses and
134 hematopoietic chemotaxis, respectively, underscoring how crosstalk between hematopoietic and
135 non-hematopoietic lineages likely contributes to infection resolution. At 12 dpi, the immune
136 landscape in fLX is characterized by an increase in CD4+ patrolling monocytes, conventional
137 dendritic cells and CD206+ interstitial macrophages (IM). Notably, systemic depletion of human
138 CD4+ cells, but not human CD3+ cells, abrogates SARS-CoV-2 clearance in fLX and causes
139 persistent infection. These findings underscore CD4+ circulating monocyte infiltration as a likely
140 feature that defines SARS-CoV-2 infection resolution.

141 Collectively, our work sheds light on a unique set of immunological events associated with
142 SARS-CoV-2 resolution in human lung tissues which dramatically contrasts with the immune
143 trajectories reported in fatal COVID-19 cases. This work opens avenues for mechanistically
144 dissecting the respective contributions of the hematopoietic and non-hematopoietic subsets
145 identified in this study, which could inform the development of immunotherapies against viral
146 respiratory diseases.

147

148 **RESULTS**

149 **BLT-L mice effectively clear SARS-CoV-2 infection following acute viral replication**

150 Previous work from our laboratory (*23*) and others (*21, 24, 25*) have shown that
151 immunodeficient mice can successfully be engrafted with human fetal lung xenograft (fLX) alone
152 or in combination with a human immune system (HIS). In this study, we leveraged a previously
153 reported mouse model co-engrafted with fetal liver and thymus as well as with human
154 hematopoietic stem cells (HSC) and fLX (BLT-L mice) (*21*). Fetal liver and thymus were engrafted
155 under the renal capsule of adult NOD.Cg-*Prkdc*$^{scid}$ *Il2rg*$^{tm1Wjl}$/SzJ (NSG) mice (12-16 weeks old)

156 prior to intravenous HSC injection. A piece of fetal lung tissue was subcutaneously engrafted on
157 the flank of each animal, as described previously (*21*) **(Fig. 1A)**. To determine the susceptibility
158 of BLT-L mice to SARS-CoV-2 infection and their ability to effectively clear infection, BLT-L mice
159 were inoculated with SARS-CoV-2 (2019-nCoV/USA_WA1/2020) via intra-graft injection. We
160 used a viral dose ($10^6$ PFU) that we previously established to drive robust and persistent infection
161 in fLX of immunodeficient mice not engrafted with a HIS (*23*) (**Fig. 1B)**.

162 Throughout the course of infection, mice did not display any weight loss (**Fig. 1C)** or
163 clinical signs of disease such as lethargy or lack of responsiveness (data not shown). To assess
164 lung histopathology and viral titers longitudinally, fLX were collected at 2, 6, and 12 dpi. Plaque
165 assay was performed on fLX homogenates to determine viral titers. A significant amount of
166 infectious viral particles could be recovered from fLX at 2 dpi (3.20 ± 2.52 log([PFU/mg of tissue]),
167 but not at 6dpi (0.281 ± 0.688 log[PFU/mg of tissue]) and 12 dpi (0.111 ± 0.293 log[PFU/mg of
168 tissue]) (**Fig. 1D**). These data demonstrated a peak of viral infection at 2 dpi, prior to resolution of
169 infection by 6 dpi. Immunohistochemistry (IHC) for SARS-CoV-2 Spike (S) protein revealed
170 infection was mainly found in the alveolar epithelium of fLX at 2 dpi (**Fig. 1E,F**). Consistent with
171 viral quantification, most viral antigen was cleared by 6 dpi and became undetectable by 12 dpi
172 (**Fig.1G,H**). SARS-CoV-2 S was primarily detected in the alveolar and bronchiole epithelium along
173 with necrotic cellular debris, consistent with the primary cell targets of SARS-CoV-2 (**Fig.1E**).
174 These findings were confirmed through IHC for SARS-CoV-2 nucleoprotein (N) at 2, 6 and 12 dpi
175 (**Fig. 1I-L**) and transmission electron microscopy (TEM) imaging of fLX at 2 dpi **(Fig. S1A-C)**.
176 Notably, TEM substantiated evidence of productive fLX infection, as indicated by the presence of
177 viral particles in the cytosol of epithelial cells and budding/invagination of virions (**Fig. S1A-C**).

178 Next, we examined histopathological phenotypes associated with active and resolved
179 infection. Interpretation of hematoxylin and eosin (H&E) staining illustrated denuding of
180 pneumocytes, neutrophil infiltration, edema, hemorrhage, thrombosis, and pneumocyte necrosis,
181 which correlated with sites of infection at 2 dpi (**Fig. 2A-E**). No major signs of histopathological

182 lung damage were observed at 6 and 12 dpi compared to naïve fLX, indicating that fLX can mount
183 repair mechanisms upon resolution of infection (**Fig. 2F-G**). A previously described semi-
184 quantitative histopathological scoring system (*23*) provided statistical confirmation for a significant
185 increase in lung pathology at 2 dpi, which was no longer apparent at 6 (**Fig. 1H**) or 12 dpi. Of
186 note, minor lung pathology was observed at baseline (naïve), likely reflecting limited graft vs. host
187 disease. Together, infection of fLX of BLT-L mice recapitulates many important hallmarks of acute
188 SARS-CoV-2 infection, including viral replication and histopathological manifestations of disease,
189 prior to effective viral clearance and lung tissue repair.
190

191 **Humoral responses do not drive SARS-CoV-2 clearance in BLT-L mice despite evidence of**
192 **Spike selective pressure.**

193 We first asked whether SARS-CoV-2 infection resolution was driven by human
194 neutralizing humoral responses. Consistent with the rapid clearance of infectious viral particles
195 by 6 dpi and the known caveat that humanized mice mount limited humoral responses (29), there
196 were no detectable neutralizing antibodies in serum collected at 2 or 12 dpi (**Fig. S2A, B**).
197 However, interestingly, genomic sequencing of virus isolated from fLX at 2 dpi revealed the
198 selection of two stable mutations in 75% of fLX (**Fig. S2C**, **Table S1**). Both mutations were located
199 in the Spike N-terminal domain (NTD): an insertion (216KLRS) and a non-synonymous mutation
200 (R245H), neither of which were present in the inoculum (**Fig. S2C**, **Table S1**). Interestingly, these
201 two mutations were found together in 100% of the viral sequences, suggesting potential co-
202 evolution (**Fig. S2D**). They have also been reported as positively selected in the context of sub-
203 optimal neutralizing antibody concentration (216KLRS) (*29*) or the context of cross-species
204 adaptation (216KLRS and R245H) (*30*). Despite lacking humoral responses, these findings reveal
205 that BLT-L mice can recapitulate host-pathogen interactions that drive SARS-CoV-2 evolution
206 and host adaptation.
207

208 **SARS-CoV-2 infection remodels the human lung cellular environment.**

209 To comprehensively map the fLX responses associated with resolution of SARS-CoV-2
210 infection, we performed single-cell RNA sequencing (scRNA-seq) on fLX from naïve BLT-L mice
211 and at 2 and 12 dpi. While most cells detected in fLX by scRNA-seq were human, a minor
212 population of mouse cells was detected, which were excluded from downstream analysis (**Fig.**
213 **S3A-C**). Initial analysis of the human compartment revealed diverse hematopoietic (T-cells/innate
214 lymphoid cells (ILC), B cells, myeloid cells and mast cells) and non-hematopoietic lineages
215 (ciliated and non-ciliated epithelial, endothelial, mesenchymal cells and chondrocytes) in both
216 naïve and infected fLX (**Fig. 3A-C and Fig. S3D,E**).

217 T-cells and innate lymphoid cells (ILC) have the same transcriptional programs, express
218 TCR genes, and play similar effector functions (*31*). Their shared features render them very
219 challenging to distinguish by scRNAseq in small datasets and without TCR sequencing
220 information (*32*). We thus considered them together as part of a T-cell/ILC population. T-cell/ILC
221 frequency dramatically decreased in fLX upon infection (naïve, 66.8%; 2 dpi, 35.3%; 12 dpi,
222 21.8%), which is consistent with evidence that COVID-19 can induce lymphoid depletion(*33, 34*)
223 (**Fig. 3B,C**). Notably, lymphopenia was not observed in the peripheral blood of BLT-L mice,
224 suggesting lymphocyte depletion in fLX was not directly attributed to declining circulating
225 peripheral lymphocytes (**Fig. S3F)**. In contrast, myeloid (naïve, 9.94%; 2 dpi, 25.3%; 12 dpi,
226 22.2%) and B-cell subsets (naïve, 3.64%; 2 dpi, 5.38%; 12 dpi, 5.31%) relatively expanded upon
227 infection (**Fig. 3B,C**). The epithelial, endothelial and mesenchymal cell frequencies increased
228 upon infection, while mast cell, ciliated cell and chondrocyte frequencies decreased (**Fig. 3B,C**).
229 Notably, most human clusters showed temporal segregation between naïve fLX and fLX at 2 and
230 12 dpi (**Fig. 3B and Fig. S3E**; naïve: black subclusters; 2 dpi: red subclusters and 12 dpi: blue
231 subclusters). This suggests that infection alters the transcriptional state of many cell types and/or
232 drives the emergence of novel cell subsets. Notably, acute infection at 2 dpi led to the emergence
233 of distinct T, myeloid, and mesenchymal cell populations, labeled as subclusters A, B, and C,

234 respectively (**Fig. 3B**). Resolved infection (12 dpi) was associated with the emergence of
235 transcriptomically distinct epithelial, endothelial, mesenchymal, B-cell and myeloid subclusters;
236 while we did not observe the emergence of transcriptomically divergent subclusters within the T-
237 cell lineages at that time point. Temporal separation of several human lineages suggests a two-
238 step tissue remodeling process during infection involving i) an initial antiviral phase mediated by
239 a limited set of human subpopulations and ii) a tissue repair phase involving a broader range of
240 human subpopulations.

241 Next, we wished to utilize scRNAseq to determine the cellular compartments enriched in
242 viral RNA. We found that viral RNA was mainly within three major lineages: mesenchymal, T-
243 cell/ILCs and myeloid (**Fig.4A,B**). AT2 and the overall epithelial compartment were not
244 significantly enriched in viral RNA despite histological evidence of epithelial infection in fLX at 2
245 dpi (**Fig. 4A and 1F,J**). Previous evidence that SARS-CoV-2 induces significant cytopathic
246 damage in AT2 cells (*35*) may suggest that infected AT2 cells are lost when undergoing the
247 scRNAseq pipeline. Within the mesenchymal cluster, viral reads were limited and distributed
248 sporadically without significant enrichment within a given subcluster (**Fig. 4B,C**). However, viral
249 RNA was strongly enriched within the 2 dpi-specific populations in the myeloid and T-cell clusters,
250 previously labeled as clusters A and B (**Fig. 4A,B**), warranting further investigations.

251

252 **Human lung epithelium signatures upon SARS-CoV-2 infection recapitulate features of**
253 **COVID-19.**

254 Subclustering of the human epithelial compartment revealed subclusters of airway basal
255 and secretory cells, alveolar type 1 (AT1) and type 2 (AT2) cells, and serous cells (**Fig. 5A**). The
256 dynamic changes of the epithelial compartment upon infection were consistent with COVID19
257 human studies (*2, 5, 36*). We noted a relative reduction of the AT2 compartment at 2 dpi (25.6%)
258 compared to naïve mice (73.1%). The AT2 compartment was partially restored at 12 dpi (49.1%)
259 (**Fig. 5B**). The frequency of basal airway cells followed a reversed trend, indirectly reflecting the

260 disruption of the AT2 compartment. The size of the AT1 compartment showed a relative increase
261 at 2 dpi (9.89% compared to 8.00% in naïve fLX), consistently with the ability of AT2 cells to
262 differentiate into AT1 upon lung damage (*37*) before returning to minimal relative levels as the
263 AT2 compartment re-expanded following infection resolution.

264 The AT2 compartment displayed the most robust remodeling upon viral infection across
265 the entire epithelial compartment, with 2 dpi and 12 dpi AT2 subclusters showing distinctive
266 transcriptomic signatures compared to naïve AT2 cells (**Fig. 5C**). Interestingly, AT2 cells did not
267 exhibit robust antiviral responses upon acute infection (**Fig. 5C**). However, they displayed gene
268 signatures previously reported during and after SARS-CoV-2 infection including, downregulation
269 of MHC genes (*HLA-C, HLA-B, and HLA-DPB1)* and *CCL5* (a cytokine associated with immune
270 recruitment during respiratory infection) (*6*), upregulation of immunomodulatory genes regulating
271 inflammation and cell stress (*SFTPA1*, *EGR1*), and elevated expression of genes associated with
272 mitochondrial dysfunctions and increased oxidative stress responses (i.e., *LARS2*). (**Fig. 5C**).
273 Activation of tissue repair mechanism (*SNHG8*) was also observed, further underscoring evidence
274 of physiologically relevant AT2 response to viral infection (**Fig. 5C**). The absence of detectable
275 viral RNA in AT2 cells was in line with the lack of antiviral responses. Such a lack of infected AT2
276 cells in our scRNAseq data is likely the reflection of their vulnerability and death during infection,
277 given histological evidence of epithelial infection (**Fig. 1F, J**) and the marked reduction of the AT2
278 compartment in fLX upon infection (**Fig. 5B**).

279 Collectively, the epithelial compartment of fLX of BLT-L mice recapitulates several
280 previously reported features of COVID-19 in humans, including loss of AT2 program,
281 downregulation of immune genes and antigen presentation, and activation of tissue repair
282 mechanisms.

283

284 **SARS-CoV-2 infection resolution is associated with the emergence of a viral RNA-enriched**
285 **double-negative T-cell subcluster with cytotoxic functions.**

286 We first aimed to characterize the T-cell signatures to SARS-CoV-2 infection resolution,
287 and with that, the features of our viral RNA-enriched, 2 dpi-specific, T-cell/ILC subcluster A. T-
288 cell/ILC responses to infection were mainly limited to this specific viral RNA-associated subcluster
289 (**Fig. 6A-D**), which segregated very distinctively from other CD3+ T-cell lineages, including
290 canonical CD4+ and CD8+ T-cells (Subcluster 6; **Fig. 6A-C**). Using doublet discriminators and
291 assessing viral RNA abundance; we determined that this subcluster was not a doublet and
292 displayed low levels of *CD4* and *CD8* transcripts, suggesting a double-negative profile, and
293 elevated levels of mitochondrial transcripts **(Fig. S4A,B**). Most notably, it was uniquely defined
294 by the expression of several transcripts known to be enriched in macrophages (*MARCO*, *TIMP1*,
295 *LYZ*), fibroblasts (*MGP*, *CALD1*, *COL1A*), or both (*A2M*, *IFITM3*) but not in T-cells (**Fig. 6E and**
296 **Fig. S4C**). This subcluster also exhibited evidence of cytotoxic function through the expression of
297 *GZMA*, *GZMB*, and *GNLY* transcripts, albeit expression was also detected in CD8+ T-cells and
298 activated tissue-resident memory T-cells (TRM) (Subclusters 1,3,4, **Fig. 6E**). Notably, a
299 subpopulation of double-negative T-cells sharing some of these cytotoxic markers has been
300 previously reported in mouse spleen(*38*). Given the proximity of this subcluster with myeloid
301 lineages (**Fig. 3A,B**) and evidence of expression of macrophage-enriched transcripts, we referred
302 to this subcluster as myeloid-like double-negative T-cells (mDNT cells). mDNT cells also exhibited
303 upregulation of key gene pathways related to COVID-19, SARS-CoV-2 cell-intrinsic immune
304 responses, cellular cytotoxicity (e.g., degranulation) and cell death, consistently with a role for this
305 subset to serve as a robust primary responder to viral infection (**Fig. 6D**). Of note, a recent human
306 challenge study reported that self-resolving SARS-CoV-2 infection is associated with non-
307 productive infection of human nasopharyngeal T-cells(*14*). In contrast, in lung autopsy samples
308 of fatal COVID-19 cases, viral RNA was enriched in myeloid cells but was not detected in T-
309 cells(*39*). Collectively, our findings underscore that the emergence of viral RNA-enriched T cell
310 populations displaying myeloid-like features in infected lung tissues is associated with effective
311 SARS-CoV-2 infection resolution.

312

313 **Transient antiviral responses by a viral RNA-enriched inflammatory monocyte subset**
314 **define lung myeloid responses driving SARS-CoV-2 infection resolution.**

315 Sub-clustering of myeloid lineages unveiled diverse subpopulations, including alveolar
316 and macrophages (AM) and IM, various monocyte subsets, and one conventional DC subset
317 (cDC) (**Fig. 7A and Fig. S5A-C**). Across all time points, monocytes represented the largest
318 sublineage, which was divided into three subgroups: naïve/resting, patrolling intravascular
319 monocytes (PIM), and inflammatory monocytes (iMO). iMO and AM were the only two subclusters
320 increasing in frequencies upon acute infection at the relative expense of cDC and IM (**Fig.7B,C**).
321 An increase in frequencies within these subclusters was associated with the emergence of
322 distinctive iMO and AM cell populations with infection-induced transcriptomic signatures,
323 underscoring a direct response of these subclusters against viral infection. Following infection
324 resolution, most iMO had phased out and frequencies of alveolar macrophages were
325 concomitantly reduced. Conjointly, the relative number of IM, cDCs and PIM increased through
326 the recruitment of cell populations with distinctive transcriptomic identities from naïve and
327 infection-associated cell populations (**Fig. 7B**, blue).

328 Despite the moderate expansion of AM at 2 dpi, iMO were the most abundant myeloid
329 lineage at 2 dpi (33.5%; **Fig. 7B, C**) and uniquely defined among other monocyte subclusters
330 through elevated expression of *VCAN, S100A8, CD14, CD163* and absence/minimal expression
331 of *CD4, MARCO and CD206 (MRC1)* (**Fig. 7D-F and Fig. S5D)**. iMO were also the leading
332 mediators of antiviral responses across all other myeloid subclusters, as exemplified by the robust
333 upregulated expression of interferon-stimulated genes (ISGs) and inflammatory cytokines (*CCL8,*
334 *CXCL10, CCL2, ISG15, DEFB1, IL1RN, IFIT1, ISG20, IFIT3,* and *MX1*), as well as inflammatory
335 markers such as *CD163* (**Fig. 7E,G**). While some ISGs (e.g., *ISG15, IFIT3, and MX1*) were
336 expressed in other myeloid lineages at 2 dpi, their expression was markedly lower compared to
337 iMO. Notably, upregulation of *CCL8*, *CXCL11* and *DEFB1* transcripts were the most exclusive to

338 iMO (**Fig. 7G**). iMO were also highly enriched in viral RNA, and corresponded to the previously
339 referred 2 dpi-specific viral RNA-enriched subcluster B (**Fig. 3B, 4B, and 7A,B,H**), which also
340 suggested an association between enrichment in viral RNA and potentiated antiviral responses.
341 Concomitantly, we examined whether viral RNA-associated iMOs (CoV-iMOs) displayed a
342 specific transcriptomic signature compared to iMOs (noCoV-iMOs) with undetectable viral RNA.
343 Notably, only two genes correlated with the presence of viral RNA in iMOs: *FGL2 and C15orf48*
344 (**Fig. 7I**). While *FGL2* was down-regulated in CoV-iMO compared to noCoV-iMOs, *C15orf48* was
345 upregulated (**Fig. 7I**). Soluble FGL2 exerts immunosuppressive functions (notably by inhibiting
346 the NF-kB pathway) (*40*). Conversely, the mitochondrial protein C15orf48 is positively regulated
347 by NF-kB signaling (*41*) and has previously been implicated in severe COVID-19, acting as a
348 positive regulator of inflammation (*42*). A recurring feature of lung monocytes in fatal cases of
349 COVID-19 is the expression of *IL-1β* (*1, 2, 6-8*), and inflammasome activation has been
350 associated with the non-productive infection of monocytes(*27*). However, no *IL-1β* expression or
351 inflammasome activation was detected in CoV-iMOs despite enrichment in viral RNA.

352 In contrast to iMO, *CD4+ CD163- CD206(MRC1)*-PIM were detectable at all time points
353 (**Sub-cluster 0**; **Fig. 7 A-C**). 2 dpi-specific PIM harbored a distinctive, intermediate transcriptomic
354 signature bridging naïve PIM and 2 dpi-specific iMO, and that was defined by the upregulation of
355 specific interferon-stimulated genes (ISGs) such as *IFI27 and XAF1*, and pro-inflammatory genes
356 (*S100A11*) (**Fig. 7J)**. At 12 dpi, PIM was the dominant subset over other monocyte subsets
357 (50.3%; **Fig. 7C**) and displayed a unique transcriptomic profile associated with anti-inflammation,
358 tissue repair and cellular debris clearance mechanisms, notably through the upregulation of
359 *FGL2, DYNLL1* and *CX3CR1*. At 12 dpi, expanded cDC and IM populations also elicited
360 comparable transcriptomic signatures.

361 mIHC analysis supported our scRNA seq findings. We observed a significant increase in
362 CD4- CD3- CD163+ cells in fLX in the extravascular interstitium and alveolar spaces, mirroring
363 the 2 dpi-specific expansion of CD4- CD163+ iMO and alveolar macrophages uncovered through

364 scRNA seq (**Fig. 7K**). CD3- CD4+ CD163- at that time point could be associated with the 2 dpi-
365 specific PIM population infiltrating the infected fLX. mIHC also recapitulated the reduction of CD3+
366 T-cells (**Fig. 7K**) at 2 dpi. At 12 dpi, fLX were still enriched in CD4+ cells, likely reflecting PIM
367 infiltration (**Fig. 7K**). CD163+ cells also persisted in fLX at 12 dpi, which can be explained by the
368 combined expansion of IM (CD4+ CD163+) and presence of AM (CD4- CD163+) at that time point
369 as CD163+ iMO phase out (**Fig. 7K**).

370 Collectively, our findings underscore a coordinated myeloid mobilization to infection
371 resolution and tissue repair, with iMO concentrating viral materials and robust antiviral responses.
372 As the viral materials are resolved, iMO populations dissipate, opening niches for other myeloid
373 lineages to engage in a coordinated tissue repair process.

374

375 **Mesenchymal and endothelial signatures of infection resolution**

376 We then examined the contribution of the mesenchymal and endothelial compartment in
377 mediating effective infection resolution. Relative expansion of the mesenchymal compartment
378 upon infection was mainly driven by an increase in fibroblast populations (**Fig. 3C; Fig. 8A,B**). An
379 increase in alveolar fibroblasts was observed at 12 dpi (49.6%; naïve=28.1%), which was
380 preceded by the emergence of a 2 dpi-specific cluster of activated fibroblasts (26.5%;
381 naïve=8.9%) (**Fig. 8A-C**), consistent with effective tissue repair in response to lung damage.
382 Activated fibroblasts were the dominant mesenchymal population in mediating antiviral responses
383 (**Fig. 8D**), as displayed by robust upregulation of major pro-inflammatory mediators such as
384 *CXCL10* and *TIMP1* (**Fig. 8F**).

385 The endothelial compartment is an important modulator of immune recruitment through
386 cytokine/chemokine signaling. Infected fLX showed the emergence of an activated, 2 dpi-specific
387 endothelial cell cluster (**Fig. 8G,H**), which was identified by increased expression of several
388 transcripts involved in myeloid chemotaxis (**Fig. 8I**), including *CXCR4* and *MCAM* (*43, 44*).
389 Notably, venous endothelial cells also displayed upregulation of a panel of interferon-stimulated

390 gene transcripts (*XAF1, IFIT1, MX1, IFI44L, RSAD2)* at 2 dpi (**Fig. 8J**) and the downregulation of
391 several transcripts coding for activation markers (*CD69*), MHC genes (*HLA-DPB1, HLA-C*) and
392 major proteins regulating cellular metabolism and transcription (*HSP90AA1, RPL13A*), which was
393 reflective of endothelial dysfunction and stress (**Fig. 8J**) consistently with human patient reports
394 and animal studies (*45-48*). Collectively, our findings support the contribution of the mesenchymal
395 and endothelium compartments in driving antiviral responses and myeloid chemotaxis,
396 respectively, in driving infection resolution.
397
398 **Systemic depletion of CD4+ cells abrogates viral clearance in fLX.**
399 Many of our findings underscore a robust association between monocyte recruitment into
400 fLX and SARS-CoV-2 infection resolution. This includes: 1) the recruitment of CD4+ PIM into
401 infected fLX, 2) the monocyte nature of iMO and of their dominant antiviral responses, 3) the high
402 enrichment in viral RNA of iMO during infection and 4) the endothelial-mediated myeloid
403 chemotaxis signature at 2 dpi. These pieces of evidence also complement recent human findings
404 which associate effective control of SARS-CoV-2 infection in the nasopharynx with monocyte
405 recruitment(*14*). Antibody-mediated depletions are commonly used to deplete specific
406 hematopoietic subsets, and they are particularly amenable to HIS mouse model studies; further
407 emphasizing the power of these *in vivo* platforms to mechanistically dissect immunological
408 mechanisms in a human context. However, no anti-human CD14 antibodies have been well
409 characterized for *in vivo* depletion of human monocytes. In contrast, anti-human CD4 antibodies
410 have been. To experimentally validate the importance of the recruitment of circulating monocytes
411 to drive infection resolution in fLX, we therefore performed systemic depletion of CD3+, CD4+,
412 and CD8+ cells through the administration of OKT3, OKT4, or OKT8 depleting antibodies,
413 respectively, via intraperitoneal injection of BLTL mice both prior to and after infection (**Fig. 9A**).
414 Human monocytes, as well as some macrophages and dendritic cells (DC) express CD4 (*49, 50*),

415 and the use of these three depleting antibodies will allow us to deconvolute the distinctive impact
416 of T-cells and monocytes in driving infection resolution.

417 Flow cytometry confirmed effective systemic depletion in the blood (**Fig. S6A**). All animals
418 were euthanized at 12 dpi to assess for the persistence of SARS-CoV-2 infection in fLX. While
419 depletion of CD3+, CD4+, and CD8+ cells induced persistent infection in some or most of the
420 animals, only CD4+ cell depletion (mean Log PFU/mg tissue = 2.37) resulted in a statistically
421 significant defect in infection resolution compared to all other experimental conditions (isotype,
422 OKT3, and OKT8-treated mice) (**Fig. 9B**). The rate of productively infected fLX was also higher
423 in CD4+ cell-depleted animals, with 72% of fLX (8/11) showing infection at 12 dpi compared to
424 50% (4/8) and 33% (2/6) in CD3- and CD8-depleted mice, respectively (**Fig. 9B**). Additionally,
425 when examining the average viral titer (Log PFU/mg of tissue) of persistently infected fLX, the
426 ones from CD4+ cell-depleted animals were significantly higher compared to CD3+ cell- depleted
427 fLX (**Fig. S6B**), furthering that CD4+ cells have a more consequential impact on driving infection
428 resolution than CD3+ cells. Anti-SARS-CoV-2 N IHC confirmed these findings and superior defect
429 of CD4+ cell-depleted animals to resolve infection (**Fig. 9C**). Using multiplex fluorescent IHC
430 (mIHC), we also validated the reduction in CD3+, CD4+ and CD3+ CD4- cells in fLX from CD3-,
431 CD4+ and CD8+ cell-depleted animals respectively, compared to isotype-treated animals
432 (**Fig.9D**). In the fLX of CD4+ cell-depleted mice, CD4+ cells depletion also associated with
433 significant reduction of CD163+ cells at 12 dpi, underscoring the association between CD4+
434 infiltration into fLX and CD163+ cell recruitment and differentiation (**Fig. 9E,F**).

435 Persistent infection in CD4+ cell-depleted animals was also associated with significant
436 downregulation of MHC class I (**Fig. 10**), a phenomenon we similarly observed in acutely infected
437 fLX (2 dpi) (**Fig. 10)** and that has been previously reported in cells with active SARS-CoV-2
438 replication (*51, 52*). This further emphasizes that depletion of CD4+ cells is associated with
439 defective viral clearance mechanisms. These findings suggest that circulating CD4-expressing
440 cells significantly mediate SARS-CoV-2 infection resolution in BLT-L mice.

441

442 **Defective monocyte recruitment is associated with systemic and local signatures of**
443 **chronic infection.**

444 To further interrogate the impact of CD4+ depletion and monocyte recruitment on SARS-
445 CoV-2 infection, we investigated fLX antiviral responses during acute and persistent infection by
446 quantifying the concentration of 32 cytokines in the peripheral blood of naïve, acutely infected,
447 persistently infected or recovered BLTL mice. Systemic levels of human CCL2 and CCL3, major
448 monocyte attractants, were elevated in CD4+ cell-depleted mice and comparable to those of
449 acutely infected mice (**Fig. 11A,B**). The maintenance of myeloid chemotaxis signals in
450 persistently infected fLX further underlines the contribution of myeloid recruitment in SARS-CoV-
451 2 infection resolution. Notably, among all cytokines and chemokines analyzed, CXCL10 was the
452 only one displaying significantly increased serum levels in acutely infected mice (2 dpi) prior to
453 returning to undetectable levels upon infection resolution (12 dpi) (**Fig 11C**). Several human
454 subsets within fLX express *CXCL10* upon acute infection, including myeloid, mesenchymal and
455 endothelial subsets (**Fig. 11D,E**). However, the myeloid compartment was the major source of
456 *CXCL10* among all human clusters at 2 dpi (**Fig. 11D,E**) and this phenotype was dominantly
457 driven by iMO (**Fig. 7G and 11E**). Therefore, our findings suggest an association between
458 circulating human CXCL10 during acute infection and the simultaneous differentiation of iMO.
459 Notably, levels of circulating human CXCL10 in persistently infected CD4+ cell-depleted mice
460 were not statistically different than those of mice that resolved infection (12 dpi) (**Fig. 11C**). These
461 results emphasize a link between persistent infection and lack of effective CXCL10 responses,
462 further strengthening a connection between monocyte recruitment, iMO antiviral responses and
463 SARS-CoV-2 infection resolution.

464 Persistently-infected mice antiviral responses were also distinguishable from acutely
465 infected (2 dpi) and isotype-treated (12 dpi) mice by elevated levels of CCL19 in serum (**Fig. 11F**).
466 CCL19 is a pro-inflammatory cytokine that has been linked with persistent viral replication and

467 inflammation such as in the context of HIV-1 infection (*53*), underlining that persistent SARS-CoV-
468 2 infection in BLT-L mice recapitulate key immunological features of chronic viral infection.
469 We have previously reported that fLX exhibit significant histopathological manifestations
470 of disease upon SARS-CoV-2 infection in the absence of an engrafted human immune system
471 (3), highlighting that tissue damage in fLX is virally induced. However, persistent infection did not
472 result in any significant histopathological manifestations of disease in fLX, which strongly
473 contrasts with acutely infected fLX (**Fig. 2H, Fig. 11G**). As minimal tissue damage is a hallmark
474 of chronic viral infection (*54*), these findings further support evidence that CD4+ cell depletion
475 promotes tissue remodeling processes underlying chronic infection and lasting viral persistence.
476

477 **DISCUSSION**

478 As our appreciation of the immunological differences between mice and humans continues
479 to grow, humanized mouse models increasingly stand out as robust platforms to understand how
480 viral pathogens interact with human tissues and the human immune system. These models are
481 especially valuable when investigating tissue and mucosal immunity since such investigations
482 remain impractical in human patients.
483 The SARS-CoV-2 pandemic has emphasized the need to increase our understanding of
484 immune mechanisms that can drive protection against immunologically novel respiratory viruses.
485 Mice engrafted with human immune systems and human lung tissues have emerged as valuable
486 tools for such investigations (*21, 23-25*), bridging the limitations of conventional animal models
487 and the challenges associated with human studies. We previously reported using the HNFL
488 mouse model that such models can be leveraged to capture immunological signatures defining
489 effective control of SARS-CoV-2 infection (*23*). However, the enhanced myeloid reconstitution of
490 the HNFL model rapidly inhibits viral replication in fLX, precluding our ability to study protective
491 naive immunological mechanisms at play upon acute and potentially symptomatic infection. This
492 study aimed to uncover novel facets of these mechanisms using a humanized mouse model that

493 exhibits robust susceptibility to acute SARS-CoV-2 infection prior resolving infection in a
494 hematopoietic-dependent manner.

495 We found that BTL-L mice are able to effectively clear infectious viral particles following
496 an early peak of viral replication in fLX. Infection resolution was associated with rapid mobilization
497 of the human immune cells into fLX upon viral inoculation, which aligns with previous evidence
498 that immunodeficient mice only engrafted with fLX are unable to clear infection (*22, 23*). Using
499 scRNAseq analysis, we identified a comprehensive network of novel factors involved in the
500 resolution of SARS-CoV-2 infection (**Fig. 12**). Our study identified three major hallmarks of this
501 process: 1) The recruitment of iMO, which display high level of enrichment in viral RNA and mount
502 dominant antiviral responses across all myeloid lineages, notably defined by CXCL10 expression;
503 2) The differentiation of mDNT cells, which are highly enriched in viral RNA and exhibit non-
504 canonical macrophage features and cytotoxic signatures; And 3) The synergistic contribution of
505 endothelial and mesenchymal cells in infection resolution via potentiating antiviral responses and
506 myeloid chemotaxis, respectively. Consistent with monocyte infiltration into infected fLX being a
507 dominant feature of our infection resolution model, systemic depletion of CD4+ cells, but not T-
508 cells, abrogated viral clearance. Persistent infection is associated with the lack of systemic
509 CXCL10 responses, dominantly mediated by iMO, as well as with signatures of chronic infection,
510 including systemic CCL19 expression and lack of fLX damage.

511 Our findings empower a recent human study reporting that protection from SARS-CoV-2
512 infection is associated with a rapid monocyte response in the nasal cavity and a decreased
513 number of circulating monocytes(*14*). Specifically, our work extends the findings of this human
514 study beyond the limitations of the human model by exploring tissue-resident events, unraveling
515 the identity of monocyte populations that extravasate tissues, differentiate and mount tissue-
516 resident immune responses to clear infection. By providing enhanced resolution on key protective
517 immunological processes and mediators that human studies alone cannot capture, our works

518 underscores how human and humanized mouse studies can effectively complement themselves
519 for improving our understanding of human antiviral immunity.
520
521 To the best of our knowledge, this study represents the initial evidence of a direct role
522 played by human lung extravascular inflammatory monocytes in the resolution of respiratory viral
523 infections. Extravascular monocytes have been proposed to serve as immune sentinels through
524 their position at the interface of the lung capillaries and alveoli (*55, 56*). However, although
525 previous research reported that these cells can promote T-cell resident memory differentiation
526 following viral infection (*57*), their direct antiviral functions have not been documented until now.
527 Four major features characterized these cells: 1) a dominant CD163-expressing population that
528 emerges during acute infection before dissipating, 2) a major source of CXCL10 expression, 3) a
529 high enrichment in viral RNA, and 4) the induction of robust antiviral responses.
530 Several lines of evidence support the monocyte nature of these cells. They display a close
531 transcriptomic relationship with patrolling monocytes, which have been reported to give rise to
532 transient, non-classical extravascular (including alveolar) monocytes in the mouse lung (*56*). The
533 iMO gene expression profile is also similar to those of human FCN1-monocytes recovered from
534 the broncho-alveolar lavage of COVID-19 patients with acute respiratory disease syndrome (*58*).
535 While further studies are needed, our data collectively suggest CD4+ PIM infiltrating the infected
536 fLX may differentiate into iMO to promote robust antiviral responses. Furthermore, our data show
537 that some iMO are negative for viral RNA, suggesting that such differentiation is independent of
538 an association with viral materials, although the presence of viral RNA could potentiate antiviral
539 responses.
540 The fate of iMO following infection resolution also remains unclear and will have to be
541 further deciphered. By 12 dpi and infection resolution, fLX display residual iMO and are enriched
542 in CD4+ PIM and CD163+ CD206+ IM. CD206+ IM are involved in response to wounding and
543 infection recovery (*56*) and CD163+ CD206+ monocyte-derived IM (*58*) have been shown to

544 directly derive from extravasating, circulating CD14+ monocytes in another human immune
545 system-engrafted mouse model (*59*). Therefore, one hypothesis would be that the pool of CD163+
546 CD206+ IM is derived both from iMO and newly recruited circulating monocytes.

547 Our findings also reveal that different monocytic fates are likely associated with distinct
548 clinical outcomes of SARS-CoV-2 infection. While our study emphasizes the protective role of
549 monocytes in preventing severe COVID-19, monocytic lineages have also been associated with
550 severe COVID-19(*2, 5, 36, 58*). Excessive monocyte infiltration, macrophage inflammation and
551 fibrotic response can lead to potentially fatal acute respiratory distress syndrome (ARDS) and
552 fibrosis despite promoting infection resolution. A suspected driver of excessive myeloid
553 inflammation is the ability of SARS-CoV-2 to trigger abortive infection of both monocytes and
554 macrophages(*27, 60-62*) through viral RNA replication and protein production, which results in
555 inflammasome activation(*27, 28, 63*). Consistently, viral RNA is enriched in inflammatory
556 monocytes and macrophages in lung autopsy samples from fatal COVID-19 cases (*5*). However,
557 our findings that viral RNA in iMO is associated with infection resolution and tissue protection
558 suggest that rapid clearance of viral RNA-enriched inflammatory monocytes, as opposed to their
559 persistence, is associated with favorable clinical outcomes.

560 Lung extravascular monocytes deriving from PIM also exhibit a dynamic transition state
561 and can differentiate into CD206- IM(*56*), primary responders to infection and important drivers of
562 inflammation. However, no CD206- macrophages were observed in infected fLX at any time point.
563 The transient presence of viral RNA-enriched iMO in fLX, leading to the absence of iMO
564 differentiation into CD206- IM, could therefore mitigate the risk of uncontrolled inflammation during
565 infection resolution. This process could prevent severe tissue damage and excessive
566 extravasation of circulating monocytes, which would otherwise differentiate into pro-fibrotic
567 CD163+ CD206+ IM, a major driver of ARDS(*58*).

568 Understanding the cellular and molecular players defining the fate of iMO upon exposure
569 to SARS-CoV-2 and how key regulatory crossroads in this subset may result in differential clinical

570 outcomes is of particular interest. Compounding immune dysregulations, such as elevated
571 inflammatory baseline and/or epigenetic imprinting related to innate immune training (*64*), may
572 hinder PIM and/or iMO's ability to adequately regulate their inflammatory responses in a timely
573 manner upon encountering viral materials or inflammatory clues. This could also favor extended
574 cell survival (NF-κB is both involved in inflammasome activation and cell survival (*65*)) and
575 subsequent differentiation into inflammatory macrophages, fostering exacerbated inflammation.
576 Our study also creates a mandate for probing the ubiquitous nature of iMO antiviral responses
577 during other respiratory viral infections and investigating more comprehensively the antiviral
578 functions of this novel subset beyond SARS-CoV-2 infection.
579
580 In parallel to ExiMO, we also identified mDNT cells, a transient DNT cell population highly
581 enriched in viral RNA and only observed upon acute infection, and which exhibits expression of
582 key macrophage-defining genes and cytotoxic markers. This population displays similarities with
583 a subpopulation of cytotoxic DNT cells previously reported in mouse spleen(*38*) and with innate-
584 like T-cells(*66*), which also harbor cytotoxic signatures. mDNT also share transcriptomic
585 similarities with γδ T-cell subsets previously described as bearing myeloid and cytotoxic
586 functions(*67, 68*). However, mDNT appear unique through a specific blend of lymphoid, and
587 conventional macrophage and mesenchymal markers and their short-lived nature (suggested by
588 their complete absence at 12 dpi). While CD8+ T-cells and macrophages isolated from
589 nasopharyngeal swabs have been identified to harbor SARS-CoV-2 RNA in human challenge
590 studies(*14*), mDNT did not meet the canonical transcriptomic signatures of these subsets,
591 suggesting the existence of tissue-resident events driving specific cellular differentiation
592 processes upon infection. Additional investigations are required to better understand the identity,
593 fate and functions of this cell subset in lung antiviral immunity. However, it is tempting to speculate
594 that mDNT may uniquely synergize CD8+ cytotoxic T-cell functions with viral particle phagocytosis
595 to effectively control infection prior to undergoing rapid cell death.

596 Despite our findings related to mDNT, the contribution of T-cells in SARS-CoV-2 infection
597 resolution remains elusive in our model. CD3+ cell depletion resulted in a partial abrogation of
598 infection resolution, with 50% of animals still capable of clearing infection. In addition, even when
599 viral infection persisted in CD3+ cell-depleted animals, viral titers in fLX remained significantly
600 lower than in the fLX of persistently infected CD4+ cell-depleted animals. One possible
601 interpretation is that T-cell depletion delays but does not abolish infection resolution. CD8+ cell-
602 depleted mice may display delayed viral clearance compared to isotype-treated mice (with
603 resolution occurring between 6dpi and 12 dpi), and CD3+ T-cell-depleted mice may be undergoing
604 progressive resolution by 12 dpi until complete clearance by a later time. In contrast, the viral titer
605 observed in fLX of CD4+ cell-depleted mice show no evidence of ongoing infection resolution.
606 How CD3+ depletion may impact mDNT differentiation, and how T-cells (including mDNT) and
607 ExiMO functions may synergize to rapidly resolve infection without extensive inflammation-
608 induced tissue damage will need further investigation.
609
610 There are inherent limitations associated with the BLT-L mouse model. First, direct viral
611 inoculation into fLX potentially bypasses key immune checkpoints in the upper respiratory tract,
612 which are not recapitulated in our model. Second, the hematopoietic reconstitution and functions
613 of the BLT-L mouse model remain imperfect, notably through the underrepresentation of specific
614 hematopoietic subsets, including dendritic cells and granulocytes, and limited B-cell responses –
615 which may ultimately bias the dynamics of viral clearance. Despite these limitations, BLT-L mice
616 recapitulated human lung responses to SARS-CoV-2 infection through AT2 loss of programming,
617 fibroblast and endothelial activation, and effective clearance of infection through robust
618 hematopoietic responses. This mouse model also supported viral adaptation processes with
619 public health relevance, and recapitulated signatures of persistent viral replication observed in
620 patients suffering from chronic infection. Our work demonstrates the potential of the BLT-L mouse
621 model to uncover naïve immune mechanisms and mediators governing the effective resolution of

622 lung infection by SARS-CoV-2 and open avenues for a comprehensive examination of such
623 processes against other viral respiratory infections, which may pave the way toward innovative
624 immunotherapy strategies against these diseases.
625

626 **AUTHOR CONTRIBUTIONS**

627 D.K., A.B.B. and F.D. conceptualized the overall study. C.H. conceptualized the computational
628 component of this study and oversaw the analysis of the single-cell RNA sequencing data. D.K.,
629 A.B.B., N.A.C. and F.D. designed the experiments. D.K., A.K.O., M.S, A.N, H.P.G., M.E., V.V.,
630 A.B.B. and F.D. performed experiments. D.K., A.K.O., A.T., J.T., M.S, A.N, P.M., M.E., J.H.C.,
631 V.V., N.A.C., C.H., A.B.B. and F.D. analyzed the data. J.T and C.H. carried out computational
632 analysis. M.E. carried out electron microscopy analysis. A.B.B. and V.V. provided access to key
633 resources. D.K. and F.D. wrote the manuscript with contributions from all authors.
634

635 **ACKNOWLEDGMENTS**

636 This work was supported in part by a start-up fund and Peter Paul Career Development
637 Professorship from Boston University (to F.D.), grants from the National Institutes of Health (K22
638 AI144050 to F.D.), Clinical and Translational Science Awards (grant UL1 TR001430) from the
639 National Center for Advancing Translational Sciences of the National Institutes of Health (to F.D.,
640 and N.A.C.) and an Evergrande MassCPR award (to NEIDL). A.B.B. was supported by
641 R01AI174875, R01AI174276, DP2DA040254, as well as CDC subcontract 200-2016-91773-
642 T.O.2. and a Massachusetts Consortium on Pathogenesis Readiness (MassCPR) grant. We also
643 thank the Evans Center for Interdisciplinary Biomedical Research at Boston University Chobanian
644 and Avedisian School of Medicine for their support of the Affinity Research Collaborative on
645 'Respiratory Viruses: A Focus on COVID19'. This work utilized a Ventana Discovery Ultra and
646 Akoya PhenoImager HT that were purchased with funding from National Institutes of Health SIG
647 grants (S10 OD026983 & S10OD030269). We thank Ronald B. Corley, NEIDL director at the time

648 of this study and MassCPR award recipient, for his constant encouragement and support for this
649 study. We thank the Boston University Animal Science Center, the Ragon Institute Human
650 Immune System Mouse core, the single cell sequencing core and microarray and sequencing
651 core, and the flow cytometry core at Boston University Chobanian and Avedisian School of
652 Medicine, and all the NEIDL animal core staff for their outstanding support. We also thank all the
653 Douam, Balazs, Connor, and Crossland lab members, NEIDL members, and members of the
654 Department of Virology, Immunology, and Microbiology and Pathology at Boston University for
655 their constant support and advice. D.K. is supported by a T32 training grant in immunology
656 (T32AI007309).
657

658 **MATERIALS AND METHODS**

659 Detailed descriptions of the materials and methods used for this study are in the Supplemental
660 Materials.
661

662 ***Institutional approvals.*** All experiments in this study, including those conducted in BSL-3, were
663 approved by an institutional biosafety committee. Animal experiments described in this study were
664 performed in accordance with protocols that were reviewed and approved by the Institutional
665 Animal Care and Use and Committee of the Ragon Institution and Boston University. All mice
666 were maintained in facilities accredited by the Association for the Assessment and Accreditation
667 of Laboratory Animal Care (AAALAC). All replication-competent SARS-CoV-2 experiments were
668 performed in a biosafety level 3 laboratory (BSL-3) at the Boston University National Emerging
669 Infectious Diseases Laboratories (NEIDL).
670

671 ***Mouse strains and sex as biological variable.*** Female NOD.Cg.-*Prkdc*$^{Scid}$*Il2rg*$^{tm1Wjl}$/SzJ (NSG)
672 mice were obtained from the Jackson Laboratory, catalog number 005557. NSG mice were
673 maintained by the Ragon Institute Human Immune System Mouse core prior to engraftment and

674 shipment to the NEIDL, Boston University. In our study, only female mice were engrafted with
675 human fetal tissues because of their ability to support higher levels of engraftment than males.
676 As we investigated human tissue responses to infection and only leveraged mice as
677 xenorecipients, the sex of the animals does represent a critical variable for our study.
678
679 ***Human fetal tissues.*** De-identified human fetal tissues were procured from Advanced Bioscience
680 Resources (Alameda, CA, USA).
681
682 ***Generation of BLT-L mice.*** BLT mice were generated via irradiation of female NOD.Cg.-
683 *Prkdc*$^{Scid}$*Il2rg*$^{tm1Wjl}$/SzJ mice (NSG mice; Jackson Laboratory #005557) prior to implantation of
684 human fetal thymic and fetal liver tissue (Advanced Bioscience Resources) under the murine
685 kidney capsula. Two pieces of homologous human fetal lung tissue were implanted into
686 subcutaneous dorsal pockets of mice. Post-implantation, mice intravenously received 1x$10^5$
687 homologous CD34+ cells. Human immune reconstitution was determined by flow cytometry at
688 weeks post-implantation. Three distinct human donors were used for this study.
689
690 ***Mouse inoculation with SARS-CoV-2.*** BLT-L mice were anesthetized with 1–3% isoflurane prior
691 to inoculation via subcutaneous, intra-fetal lung xenograft (intra-fLX) injection with $10^6$ plaque
692 forming unites (PFU) of SARS-CoV-2 WA-1 isolate in 50 µL of sterile 1X PBS. Mice were
693 euthanized at 2-, 6-, and 12-days post inoculation.
694
695 ***In vivo antibody depletion.*** BLT-L mice were administered 200 mg of anti-CD3e (OKT3)
696 (BioxCell; cat. # BE0001-2), anti-CD4 (OKT4) (BioxCell; cat. # BE0003-2), anti-CD8 (OKT8)
697 (BioxCell; cat. # BE0004-2), or isotype IgG2a (Thermofisher; cat # 02-6200) antibody 3-, 2-, and
698 1-day prior to inoculation and 4- and 8-days post inoculation with 1x$10^6$ PFU SARS-CoV-2 WA-
699 1.

700

701 ***Quantification and statistical Analysis.*** For histopathological score and viral load/titer
702 comparisons a Kruskla-Wallis, non-parametric one-way ANOVA with Benjamini, Krieger, and
703 Yekutieli correction for multiple comparisons was applied given the non-continuous nature of the
704 data. For cytokine data, an Ordinary one-way ANOVA with uncorrected Fishers LSD was used
705 as the data was collected from different time points, treatment conditions, and cohorts. A Kruskla-
706 Wallis, non-parametric one-way ANOVA with an uncorrected Dunn's test was applied for CD163+
707 Area quantification (AQ) due to the independent comparisons between the samples. All statistical
708 tests and graphical depictions of results were performed using GraphPad Prism version 9.0.1
709 software (GraphPad Software, La Jolla, CA). For all tests, $p \leq 0.05$ was considered statistically
710 significant. Statistical significance on figures and supplemental figures is labeled with p-values
711 and non-significant values are labeled with n.s. or left unlabeled.

712

713 ***Data availability***. The Genome Expression Omnibus (GEO) accession number to access the raw
714 data of our scRNAseq analysis is GSE255200.

715

716 **REFERENCES**


717 1. J. C. Melms *et al.*, A molecular single-cell lung atlas of lethal COVID-19. *Nature* **595**, 114-
718 119 (2021).
719 2. A. F. Rendeiro *et al.*, The spatial landscape of lung pathology during COVID-19
720 progression. *Nature* **593**, 564-569 (2021).
721 3. E. Wauters *et al.*, Discriminating mild from critical COVID-19 by innate and adaptive
722 immune single-cell profiling of bronchoalveolar lavages. *Cell Res* **31**, 272-290 (2021).
723 4. R. A. Grant *et al.*, Circuits between infected macrophages and T cells in SARS-CoV-2
724 pneumonia. *Nature* **590**, 635-641 (2021).
725 5. T. M. Delorey *et al.*, COVID-19 tissue atlases reveal SARS-CoV-2 pathology and cellular
726 targets. *Nature*, (2021).
727 6. M. Liao *et al.*, Single-cell landscape of bronchoalveolar immune cells in patients with
728 COVID-19. *Nat Med* **26**, 842-844 (2020).
729 7. X. Ren *et al.*, COVID-19 immune features revealed by a large-scale single-cell
730 transcriptome atlas. *Cell* **184**, 5838 (2021).
731 8. P. A. Szabo *et al.*, Longitudinal profiling of respiratory and systemic immune responses
732 reveals myeloid cell-driven lung inflammation in severe COVID-19. *Immunity* **54**, 797-814
733 e796 (2021).

9. S. S. Batah, A. T. Fabro, Pulmonary pathology of ARDS in COVID-19: A pathological review for clinicians. *Respir Med* **176**, 106239 (2021).
10. C. Fan *et al.*, Animal models for COVID-19: advances, gaps and perspectives. *Signal Transduct Target Ther* **7**, 220 (2022).
11. E. Stephenson *et al.*, Single-cell multi-omics analysis of the immune response in COVID-19. *Nat Med* **27**, 904-916 (2021).
12. X. Ren *et al.*, COVID-19 immune features revealed by a large-scale single-cell transcriptome atlas. *Cell* **184**, 1895-1913 e1819 (2021).
13. R. Edahiro *et al.*, Single-cell analyses and host genetics highlight the role of innate immune cells in COVID-19 severity. *Nat Genet* **55**, 753-767 (2023).
14. R. G. H. Lindeboom *et al.*, Human SARS-CoV-2 challenge uncovers local and systemic response dynamics. *Nature*, (2024).
15. D. G. Augusto *et al.*, A common allele of HLA is associated with asymptomatic SARS-CoV-2 infection. *Nature* **620**, 128-136 (2023).
16. C. G. K. Ziegler *et al.*, Impaired local intrinsic immunity to SARS-CoV-2 infection in severe COVID-19. *Cell* **184**, 4713-4733 e4722 (2021).
17. M. Dugas *et al.*, Less severe course of COVID-19 is associated with elevated levels of antibodies against seasonal human coronaviruses OC43 and HKU1 (HCoV OC43, HCoV HKU1). *Int J Infect Dis* **105**, 304-306 (2021).
18. M. Sagar *et al.*, Recent endemic coronavirus infection is associated with less-severe COVID-19. *J Clin Invest* **131**, (2021).
19. K. Medetgul-Ernar, M. M. Davis, Standing on the shoulders of mice. *Immunity* **55**, 1343-1353 (2022).
20. A. Rongvaux *et al.*, Human hemato-lymphoid system mice: current use and future potential for medicine. *Annu Rev Immunol* **31**, 635-674 (2013).
21. A. Wahl *et al.*, Precision mouse models with expanded tropism for human pathogens. *Nat Biotechnol* **37**, 1163-1173 (2019).
22. A. Wahl *et al.*, SARS-CoV-2 infection is effectively treated and prevented by EIDD-2801. *Nature* **591**, 451-457 (2021).
23. D. J. Kenney *et al.*, Humanized mice reveal a macrophage-enriched gene signature defining human lung tissue protection during SARS-CoV-2 infection. *Cell Rep* **39**, 110714 (2022).
24. Y. Di *et al.*, SARS-CoV-2 Variant-Specific Infectivity and Immune Profiles Are Detectable in a Humanized Lung Mouse Model. *Viruses* **14**, (2022).
25. R. Sun *et al.*, Humanized mice for investigating SARS-CoV-2 lung infection and associated human immune responses. *Eur J Immunol* **52**, 1640-1647 (2022).
26. L. Baena Carstens *et al.*, Lung Inflammasome Activation in SARS-CoV-2 Post-Mortem Biopsies. *Int J Mol Sci* **23**, (2022).
27. C. Junqueira *et al.*, FcgammaR-mediated SARS-CoV-2 infection of monocytes activates inflammation. *Nature* **606**, 576-584 (2022).
28. E. Sefik *et al.*, Inflammasome activation in infected macrophages drives COVID-19 pathology. *Nature* **606**, 585-593 (2022).
29. PMDA, Xevudy for Intravenous Infusion 500 mg_GlaxoSmithKline K.K._Report on Special Approval for Emergency; https://www.pmda.go.jp/files/000245006.pdf. (2021).
30. A. Fagre *et al.*, SARS-CoV-2 infection, neuropathogenesis and transmission among deer mice: Implications for spillback to New World rodents. *PLoS Pathog* **17**, e1009585 (2021).
31. C. Harly, M. Cam, J. Kaye, A. Bhandoola, Development and differentiation of early innate lymphoid progenitors. *J Exp Med* **215**, 249-262 (2018).
32. G. Pizzolato *et al.*, Single-cell RNA sequencing unveils the shared and the distinct cytotoxic hallmarks of human TCRVdelta1 and TCRVdelta2 gammadelta T lymphocytes. *Proc Natl Acad Sci U S A* **116**, 11906-11915 (2019).

785 33. Q. Zhao *et al.*, Lymphopenia is associated with severe coronavirus disease 2019 (COVID-
786 19) infections: A systemic review and meta-analysis. *Int J Infect Dis* **96**, 131-135 (2020).
787 34. S. Tavakolpour, T. Rakhshandehroo, E. X. Wei, M. Rashidian, Lymphopenia during the
788 COVID-19 infection: What it shows and what can be learned. *Immunol Lett* **225**, 31-32
789 (2020).
790 35. J. Huang *et al.*, SARS-CoV-2 Infection of Pluripotent Stem Cell-Derived Human Lung
791 Alveolar Type 2 Cells Elicits a Rapid Epithelial-Intrinsic Inflammatory Response. *Cell stem*
792 *cell* **27**, 962-+ (2020).
793 36. E. Wauters *et al.*, Discriminating mild from critical COVID-19 by innate and adaptive
794 immune single-cell profiling of bronchoalveolar lavages. *Cell Res* **31**, 272-290 (2021).
795 37. A. Wu, H. Song, Regulation of alveolar type 2 stem/progenitor cells in lung injury and
796 regeneration. *Acta Biochim Biophys Sin (Shanghai)* **52**, 716-722 (2020).
797 38. L. Yang *et al.*, Transcriptome landscape of double negative T cells by single-cell RNA
798 sequencing. *J Autoimmun* **121**, 102653 (2021).
799 39. T. M. Delorey *et al.*, A single-cell and spatial atlas of autopsy tissues reveals pathology
800 and cellular targets of SARS-CoV-2. *bioRxiv*, 2021.2002.2025.430130 (2021).
801 40. L. Fu, Z. Liu, Y. Liu, Fibrinogen-like protein 2 in inflammatory diseases: A future
802 therapeutic target. *Int Immunopharmacol* **116**, 109799 (2023).
803 41. Y. Takakura *et al.*, Mitochondrial protein C15ORF48 is a stress-independent inducer of
804 autophagy that regulates oxidative stress and autoimmunity. *Nat Commun* **15**, 953 (2024).
805 42. S. A. Clayton *et al.*, Inflammation causes remodeling of mitochondrial cytochrome c
806 oxidase mediated by the bifunctional gene C15orf48. *Sci Adv* **7**, eabl5182 (2021).
807 43. S. K. Gupta, P. G. Lysko, K. Pillarisetti, E. Ohlstein, J. M. Stadel, Chemokine receptors in
808 human endothelial cells. Functional expression of CXCR4 and its transcriptional regulation
809 by inflammatory cytokines. *J Biol Chem* **273**, 4282-4287 (1998).
810 44. A. S. Leroyer *et al.*, CD146 (Cluster of Differentiation 146). *Arterioscler Thromb Vasc Biol*
811 **39**, 1026-1033 (2019).
812 45. H. M. Otifi, B. K. Adiga, Endothelial Dysfunction in Covid-19 Infection. *Am J Med Sci* **363**,
813 281-287 (2022).
814 46. Z. Qin *et al.*, Endothelial cell infection and dysfunction, immune activation in severe
815 COVID-19. *Theranostics* **11**, 8076-8091 (2021).
816 47. T. Kadiyska *et al.*, Role of endothelial dysfunction in the severity of COVID-19 infection
817 (Review). *Molecular medicine reports* **26**, (2022).
818 48. S. W. Xu, I. Ilyas, J. P. Weng, Endothelial dysfunction in COVID-19: an overview of
819 evidence, biomarkers, mechanisms and potential therapies. *Acta Pharmacol Sin* **44**, 695-
820 709 (2023).
821 49. A. Zhen *et al.*, CD4 ligation on human blood monocytes triggers macrophage
822 differentiation and enhances HIV infection. *J Virol* **88**, 9934-9946 (2014).
823 50. L. Jardine *et al.*, Rapid detection of dendritic cell and monocyte disorders using CD4 as a
824 lineage marker of the human peripheral blood antigen-presenting cell compartment. *Front*
825 *Immunol* **4**, 495 (2013).
826 51. N. Arshad *et al.*, SARS-CoV-2 accessory proteins ORF7a and ORF3a use distinct
827 mechanisms to down-regulate MHC-I surface expression. *Proc Natl Acad Sci U S A* **120**,
828 e2208525120 (2023).
829 52. J. S. Yoo *et al.*, SARS-CoV-2 inhibits induction of the MHC class I pathway by targeting
830 the STAT1-IRF1-NLRC5 axis. *Nat Commun* **12**, 6602 (2021).
831 53. J. K. Damas *et al.*, Homeostatic chemokines CCL19 and CCL21 promote inflammation in
832 human immunodeficiency virus-infected patients with ongoing viral replication. *Clin Exp*
833 *Immunol* **157**, 400-407 (2009).
834 54. E. I. Zuniga, M. Macal, G. M. Lewis, J. A. Harker, Innate and Adaptive Immune Regulation
835 During Chronic Viral Infections. *Annu Rev Virol* **2**, 573-597 (2015).

55. M. P. Rodero *et al.*, Immune surveillance of the lung by migrating tissue monocytes. *Elife* **4**, e07847 (2015).
56. J. Schyns *et al.*, Non-classical tissue monocytes and two functionally distinct populations of interstitial macrophages populate the mouse lung. *Nat Commun* **10**, 3964 (2019).
57. P. R. Dunbar *et al.*, Pulmonary monocytes interact with effector T cells in the lung tissue to drive T(RM) differentiation following viral infection. *Mucosal Immunol* **13**, 161-171 (2020).
58. D. Wendisch *et al.*, SARS-CoV-2 infection triggers profibrotic macrophage responses and lung fibrosis. *Cell* **184**, 6243-6261 e6227 (2021).
59. E. Evren *et al.*, Distinct developmental pathways from blood monocytes generate human lung macrophage diversity. *Immunity* **54**, 259-275 e257 (2021).
60. J. Zheng *et al.*, Severe Acute Respiratory Syndrome Coronavirus 2-Induced Immune Activation and Death of Monocyte-Derived Human Macrophages and Dendritic Cells. *J Infect Dis* **223**, 785-795 (2021).
61. A. Boumaza *et al.*, Monocytes and Macrophages, Targets of Severe Acute Respiratory Syndrome Coronavirus 2: The Clue for Coronavirus Disease 2019 Immunoparalysis. *J Infect Dis* **224**, 395-406 (2021).
62. D. Yang *et al.*, Attenuated Interferon and Proinflammatory Response in SARS-CoV-2-Infected Human Dendritic Cells Is Associated With Viral Antagonism of STAT1 Phosphorylation. *J Infect Dis* **222**, 734-745 (2020).
63. D. Munnur *et al.*, Altered ISGylation drives aberrant macrophage-dependent immune responses during SARS-CoV-2 infection. *Nat Immunol* **22**, 1416-1427 (2021).
64. J. Ochando, W. J. M. Mulder, J. C. Madsen, M. G. Netea, R. Duivenvoorden, Trained immunity - basic concepts and contributions to immunopathology. *Nat Rev Nephrol* **19**, 23-37 (2023).
65. M. Mussbacher, M. Derler, J. Basilio, J. A. Schmid, NF-kappaB in monocytes and macrophages - an inflammatory master regulator in multitalented immune cells. *Front Immunol* **14**, 1134661 (2023).
66. M. Molgora, M. Colonna, Innate-like T cells: A promising asset in anti-cancer immunity. *Cancer Cell* **40**, 714-716 (2022).
67. M. Lebedev, B. Faburay, J. A. Richt, A. Young, Myeloid-like gammadelta T cell subset in the immune response to an experimental Rift Valley fever vaccine in sheep. *Vet Immunol Immunopathol* **233**, 110184 (2021).
68. M. Muto, M. Baghdadi, R. Maekawa, H. Wada, K. Seino, Myeloid molecular characteristics of human gammadelta T cells support their acquisition of tumor antigen-presenting capacity. *Cancer Immunol Immunother* **64**, 941-949 (2015).

## FIGURES

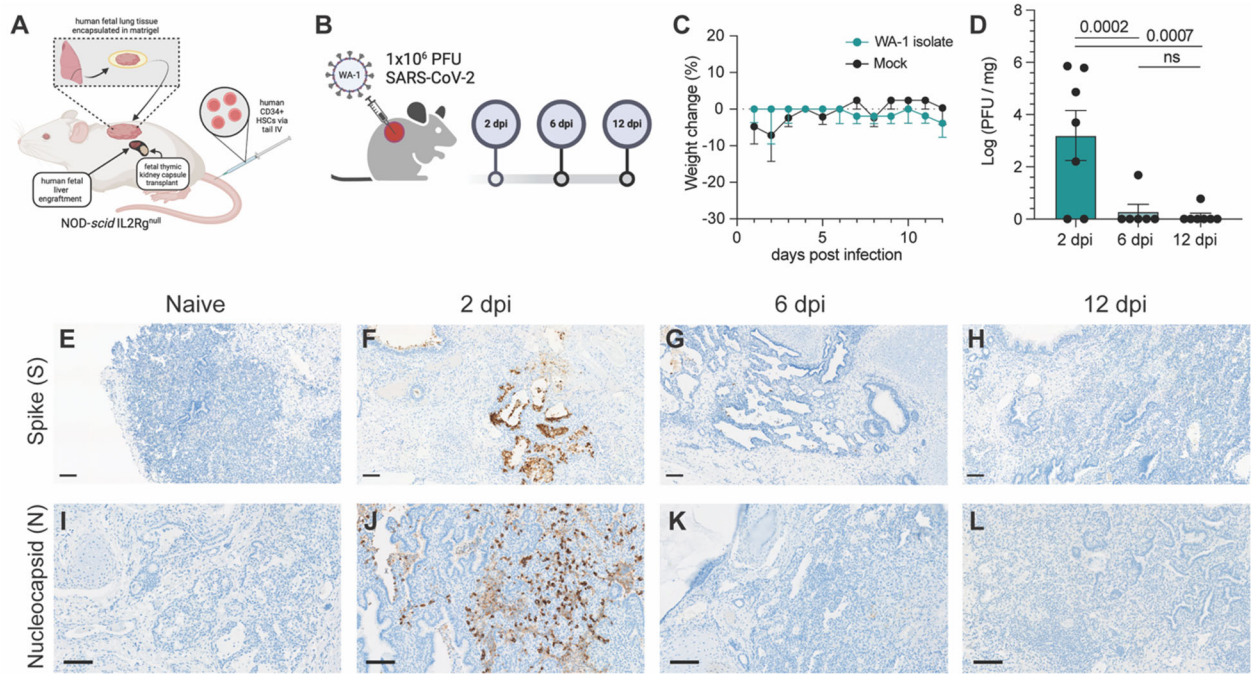


**Figure 1. BLT-L mice effectively resolve SARS-CoV-2 infection. (A)** Representative schematic of BLT-L mice. **(B)** Fetal lung xenografts (fLX) of BLT-L mice were infected with $1x10^6$ PFU of SARS-CoV-2 WA-1 isolate via subcutaneous intra-graft injection. **(C)** BLT-L mice were monitored for weight change over the course of 12 days post-infection (dpi). **(D)** Viral titer (log(PFU/mg)) in fLX at 2, 6, and 12 dpi as determined by plaque assay. **(E-H)** Immunohistochemistry for SARS-CoV-2 S and **(I-L)** N protein were performed on naïve fLX **(E,I)** and fLX at 2 dpi **(F,J)**, 6dpi **(G,K),** and 12 dpi **(H,L)**. Scale bar = 100 μM. Data are representative of two or three independent experiments. n = 6 -10 per timepoint. Error bars represent mean ± standard error of the mean. *One-way ANOVA analysis was performed. p-values are indicated. n.s. = non-significant.*

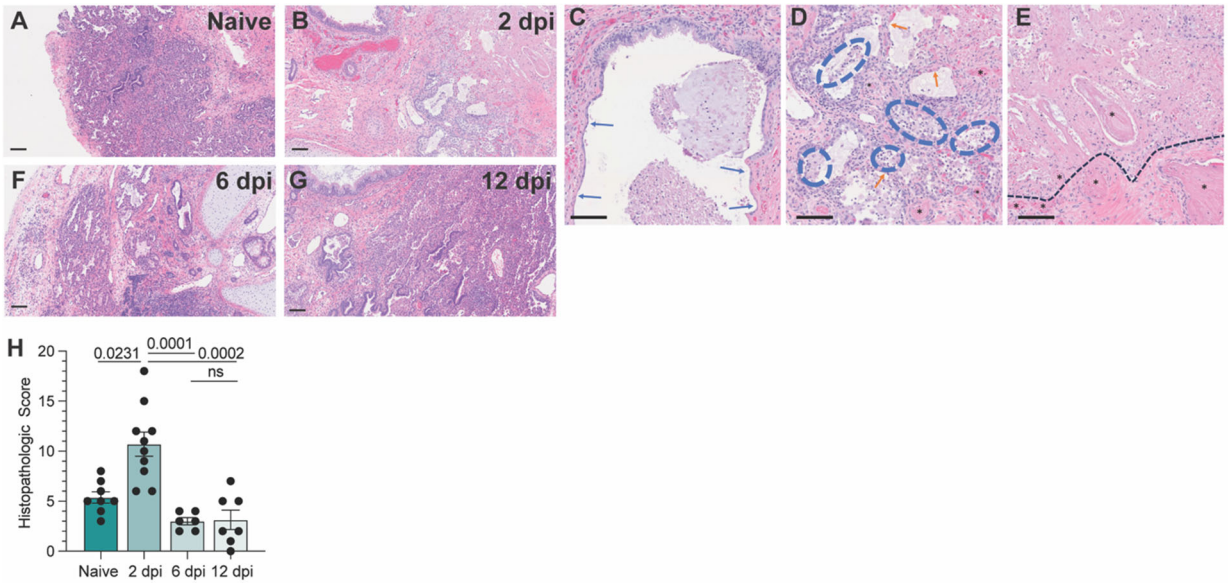


**Figure 2. BLT-L mice resolve histopathological damage in fLX. (A-E)** Hematoxylin and eosin staining was performed on naïve fLX **(A)** and fLX at 2 dpi **(B-E)**, 6dpi **(F),** and 12 dpi **(G)**. Scale bar = 100 μM. **(C)** Bronchiolar attenuation and denuding (blue arrows) correlates directly with the presence of SARS-CoV-2 Spike protein. **(D)** Alveolar spaces are multifocally filled with necrotic debris admixed with neutrophils and edema (blue hashes). Type II pneumocytes (ATII) are often denuded or attenuated in areas of inflammation that correlates directly with the presence of SARS-CoV-2 Spike protein. Fibrin thrombi are routinely observed in neighboring parenchyma (black asterisks). **(E)** Coagulative necrosis as evidenced by loss of cellular detail and generalized eosinophilia (above the black hashed line) with numerous regional fibrin thrombi (black asterisks). Although SARS-CoV-2 Spike protein is not observed in the area of coagulative necrosis viral antigen is located within adjacent tissue. **(H)** Histopathological scoring of naïve fLX and fLX at 2, 6, and 12 dpi. Data are representative of two or three independent experiments. n = 6 -10 per timepoint. Error bars represent mean ± standard error of the mean. *One-way ANOVA analysis was performed. p-values are indicated. n.s. = non-significant.*

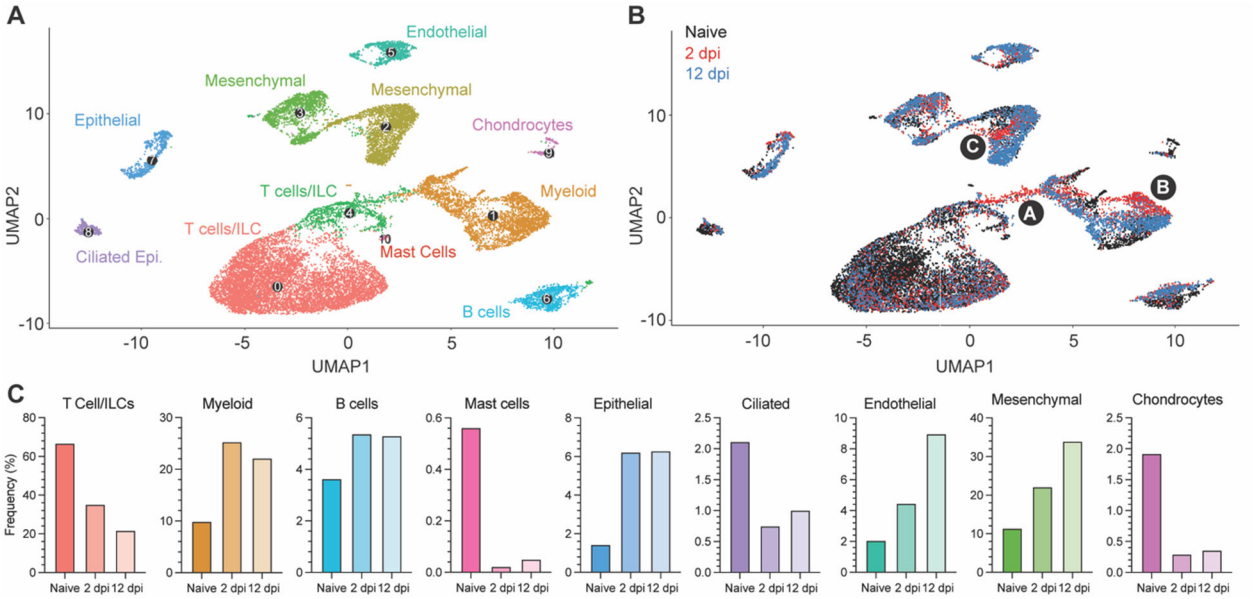


**Figure 3**. **Cellular remodeling and viral dynamics in fLX upon SARS-CoV-2 infection**

Single cell RNA sequencing analysis was performed on single cell suspensions of naïve fLX and fLX at 2 and 12 dpi. Naïve n=3 fLX (9,605 cells), 2 dpi n=2 fLX (4,405 cells), and 12 dpi n = 2 fLX (5,857 cells). **(A)** UMAP plot clustering of the human cell compartment of naïve fLX and fLX at 2 and 12 dpi. **(B)** Temporal annotation of the human clusters on the UMAP plot: naïve (black), 2 dpi (red), 12 dpi (blue). Sub-clusters unique to 2 dpi are annotated by A (T cell compartment), B (myeloid compartment) and C (mesenchymal compartment). **(C)** Frequency of each cell compartment determined by single cell RNA-sequencing.

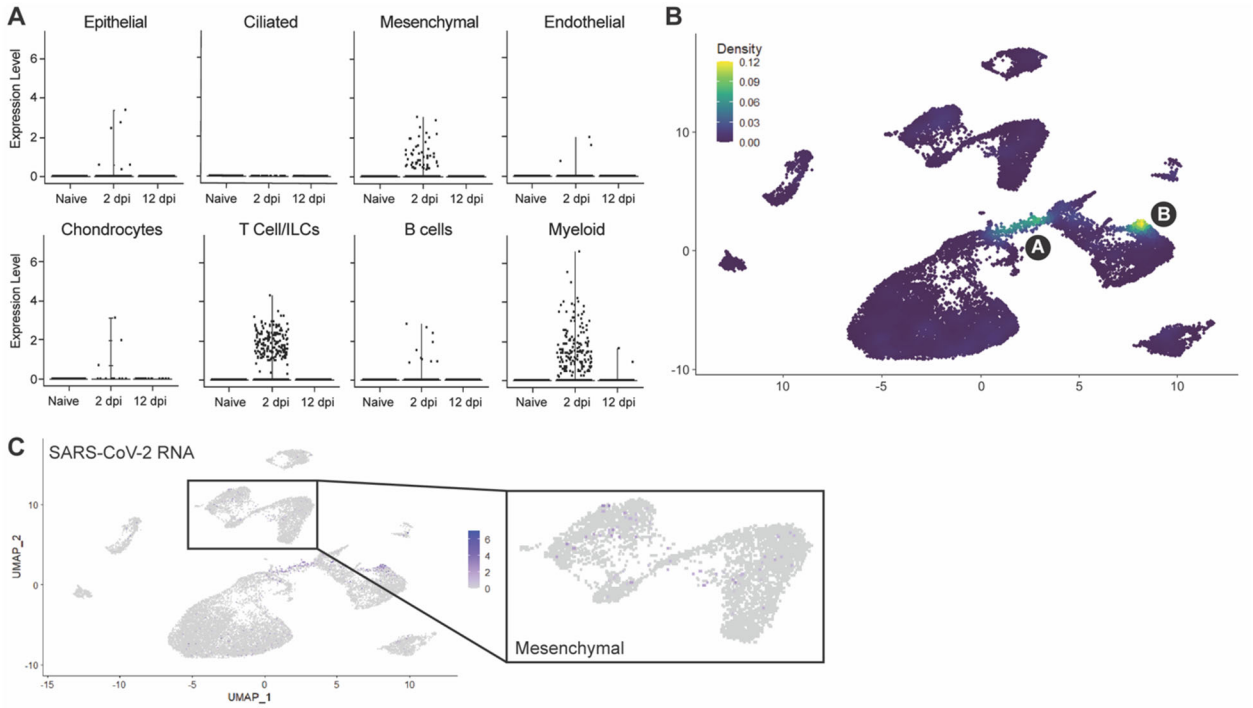


**Figure 4. Cellular compartmentalization of viral RNA during infection. (A)** Dot plots displaying the expression of SARS-CoV-2 viral RNA transcripts identified in scRNA-seq. **(B)** UMAP plot showing the distribution of SARS-CoV-2 viral RNA transcripts by density across all human cell clusters and time points. **(C)** UMAP plot showing the distribution of SARS-CoV-2 viral RNA reads across all human cell clusters and time points. Inset showing distribution of viral RNA reads in the mesenchymal cluster.

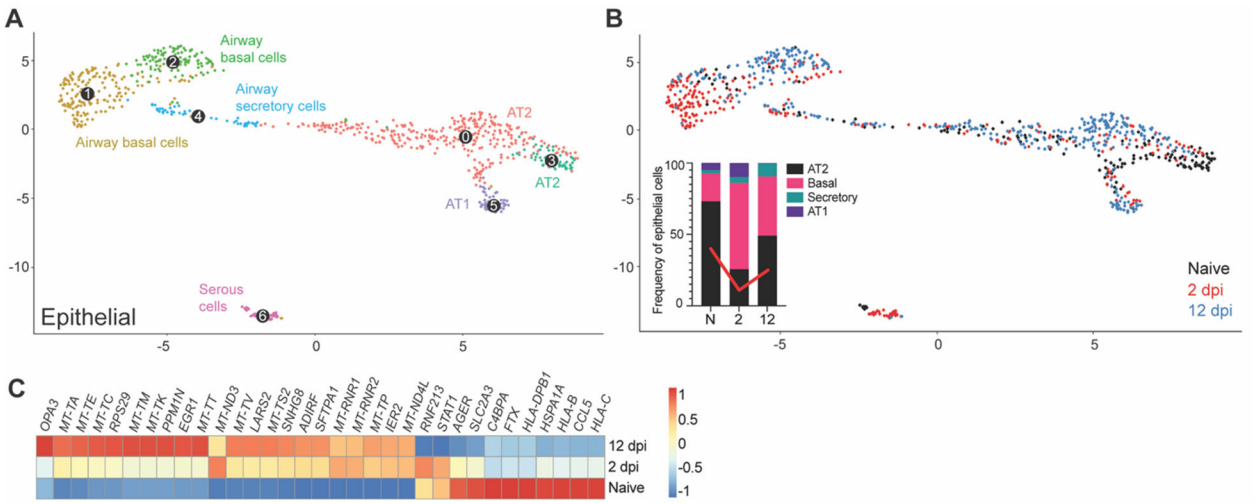


**Figure 5. Remodeling of the epithelial compartment of fLX during infection. (A)** UMAP plot sub-clustering of the human epithelial compartment in fLX across all time points. **(B)** Temporal annotation of the human epithelial sub-clusters on the UMAP plot: naïve (black), 2 dpi (red), 12 dpi (blue). The inset graph indicates the change in frequency of each compartment (AT2; black, Basal; pink, Secretory; teal, and AT1; purple) within the epithelial compartment. Red line indicates the change in the AT2 compartment over time. **(C)** Heatmap displaying the relative expression (from -1 to 1) of the top differentially regulated genes over the course of infection within the AT2 compartment.

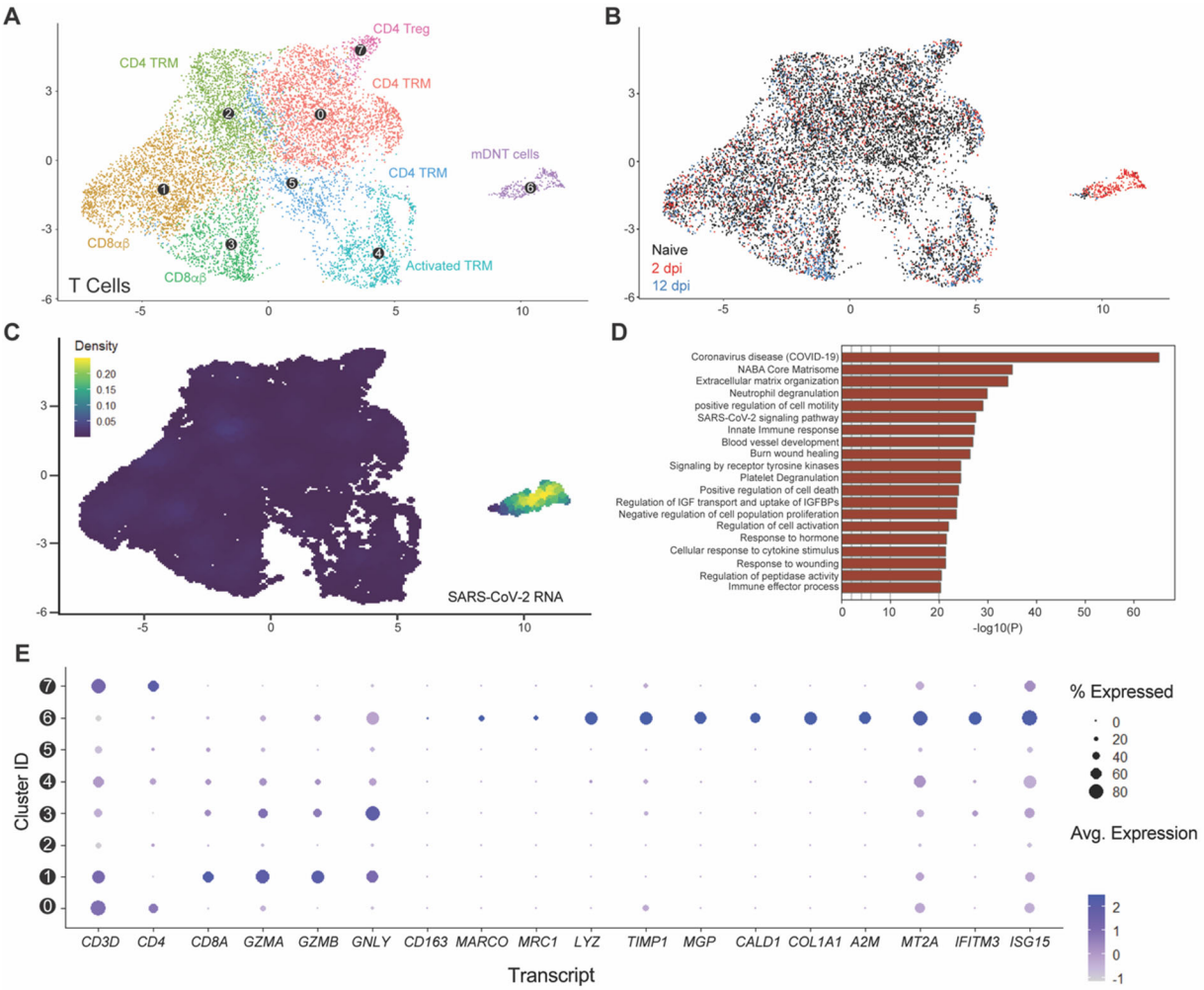


**Figure 6. Myeloid-like double-negative T-cell emerges upon acute infection and are enriched in viral RNA. (A)** UMAP plot showing the sub-clustering of the human T-cell compartment of fLX across all time points. **(B)** Temporal annotation of the human T-cell sub-clusters on the UMAP plot: naïve (black), 2 dpi (red),2 dpi (blue). **(C)** UMAP plot (all time points) showing the distribution of SARS-CoV-2 viral RNA transcripts in the T-cell compartment. **(D)** Go-term analysis showing the most highly upregulated signaling pathways in the mDNT (sub-cluster 6). **(E)** Relative expression of T cells, macrophage, mesenchymal and antiviral markers within each of the T-cell sub-clusters (From 0 to 7; as labeled in panel A).

967

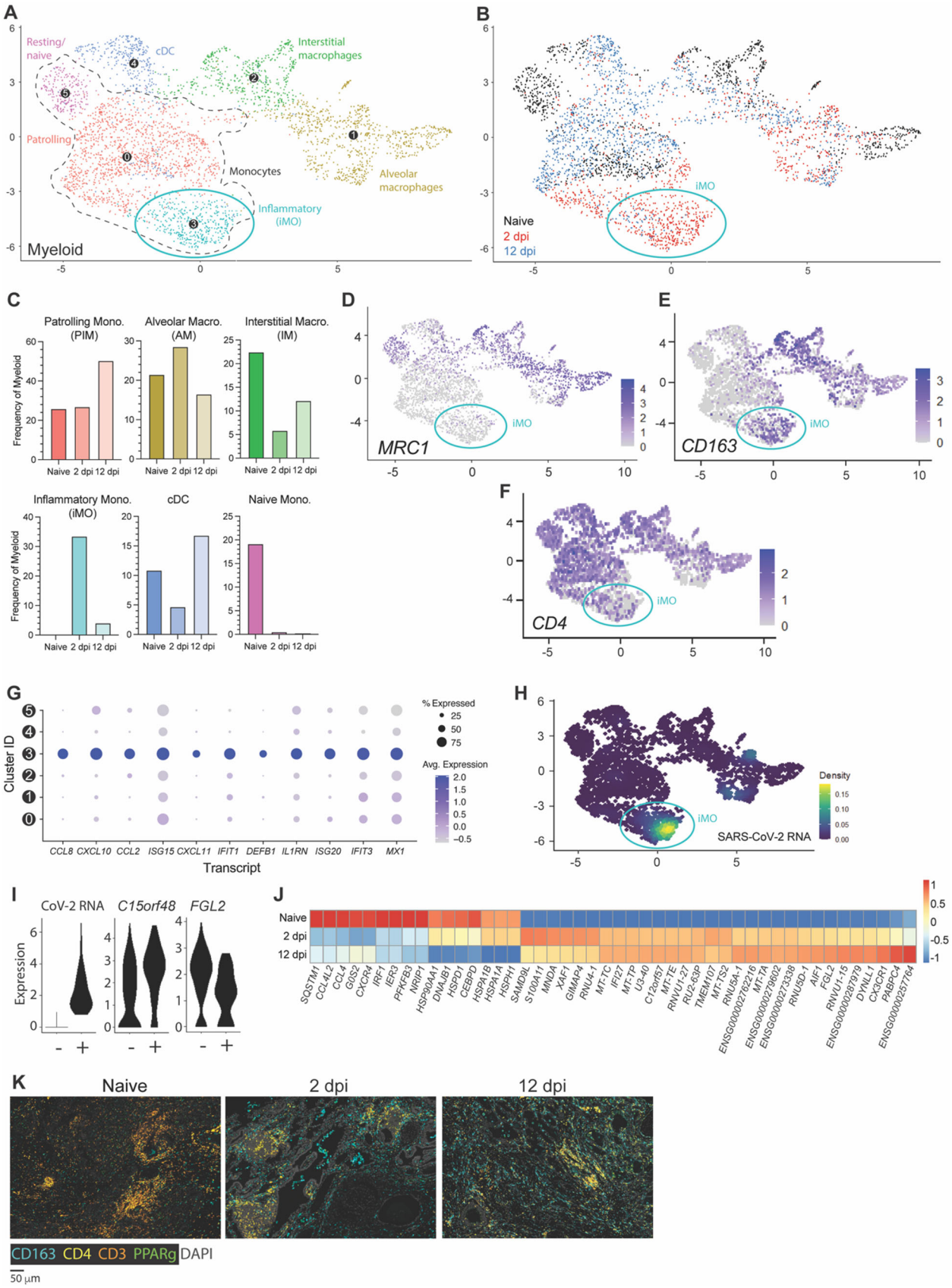
A
Resting/ naive
cDC
Interstitial macrophages
Patrolling
Monocytes
Alveolar macrophages
Inflammatory (iMO)
Myeloid
B
iMO
Naive
2 dpi
12 dpi
C
Patrolling Mono. (PIM)
Alveolar Macro. (AM)
Interstitial Macro. (IM)
Inflammatory Mono. (iMO)
cDC
Naive Mono.
Frequency of Myeloid
Naive 2 dpi 12 dpi
D
MRC1
E
CD163
F
CD4
G
Cluster ID
% Expressed
Avg. Expression
CCL8 CXCL10 CCL2 ISG15 CXCL11 IFIT1 DEFB1 IL1RN ISG20 IFIT3 MX1
Transcript
H
Density
SARS-CoV-2 RNA
I
CoV-2 RNA
C15orf48
FGL2
Expression
J
Naive
2 dpi
12 dpi
K
Naive
2 dpi
12 dpi
CD163 CD4 CD3 PPARg DAPI
50 µm

968 **Figure 7. CD163+ extravascular inflammatory monocytes arise during acute viral infection**
969 **and are predominant antiviral mediators. (A)** UMAP plot showing sub-clustering of the human
970 myeloid compartment of fLX across all time points. **(B)** Temporal annotation of the myeloid sub-
971 clusters on the UMAP plot: naïve (black), 2 dpi (red), 12 dpi (blue). iMO sub-cluster is indicated
972 with a blue circle. **(C)** Frequency of each myeloid sub-cluster by timepoint. **(D-F)** UMAP plot
973 showing the expression of *MRC1* **(D)**, CD*163* **(E)**, and *CD4* **(F)** across myeloid sub-sets. **(G)**
974 Relative expression of highly upregulated ISGs and inflammatory markers in each of the myeloid
975 sub-clusters. **(H)** UMAP plot (all time points) showing the distribution of SARS-CoV-2 viral RNA
976 transcripts in the myeloid compartment. **(I)** Violin plots showing expression level of differentially
977 expressed genes between SARS-CoV-2 positive and negative ExiMO (sub-cluster 3). **(J)**
978 Heatmap displaying the relative expression (from -1 to 1) of the top differentially regulated genes
979 over the course of infection within the patrolling monocyte (0) compartment. **(K)** Multiplex
980 fluorescent immunohistochemistry of naïve fLX and fLX at 2 and 12 dpi. CD163: teal, CD4: yellow,
981 CD3: orange, PPARγ: green, Dapi: gray. Two representative images. Scale bar = 100 μM.
982

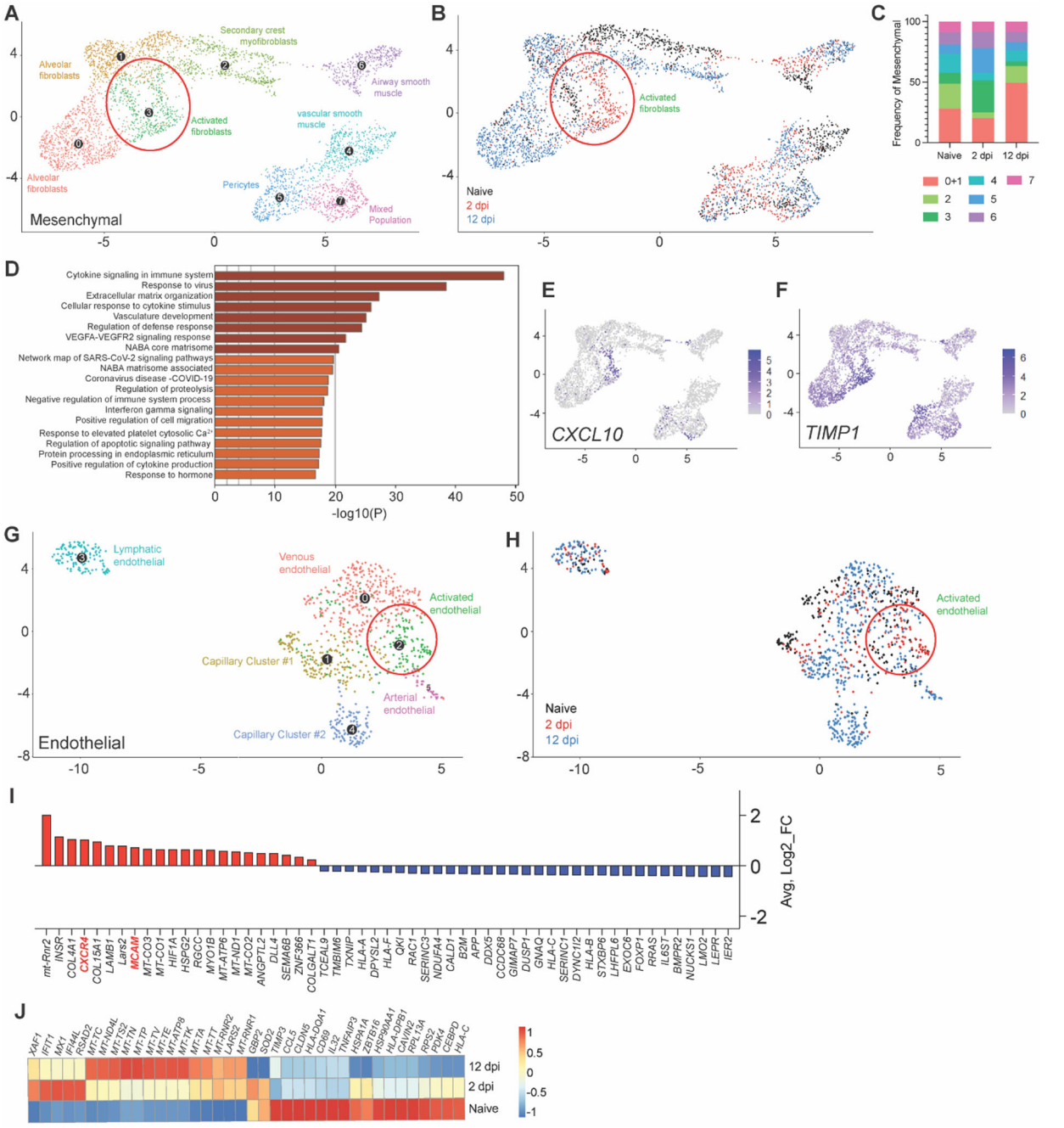


**Figure 8. (A)** UMAP plot sub-clustering of the human mesenchymal compartment in fLX across all time points. **(B)** Temporal annotation of the mesenchymal sub-clusters on the UMAP plot: naïve (black), 2 dpi (red), 12 dpi (blue). **(C)** Frequency of mesenchymal sub-clusters. **(D)** Go-term analysis showing cellular pathways linked to significantly upregulated genes within the activated

989 fibroblasts sub-cluster. **(E-F)** UMAP plot showing *CXCL10* **(E)** and *TIMP1* **(F)** expression within
990 all human mesenchymal sub-clusters and across all time points. Activated fibroblasts are
991 indicated by a red circle in A and B. **(G)** UMAP plot sub-clustering of the human endothelial
992 compartment of fLX across all time points. **(H)** Temporal annotation of the endothelial sub-clusters
993 on the UMAP plot: naïve (black), 2 dpi (red), 12 dpi (blue). **(I)** List of upregulated (red) and
994 downregulated (blue) genes specific to the activated endothelial sub-cluster (Cluster 2) over the
995 other endothelial sub-clusters (*p.adj*≤0.05). **(J)** Heatmap displaying the relative expression (from
996 -1 to 1) of the top differentially regulated genes over the course of infection within the venous
997 endothelial compartment.
998
999
1000
1001
1002
1003
1004
1005
1006
1007
1008
1009
1010
1011
1012
1013

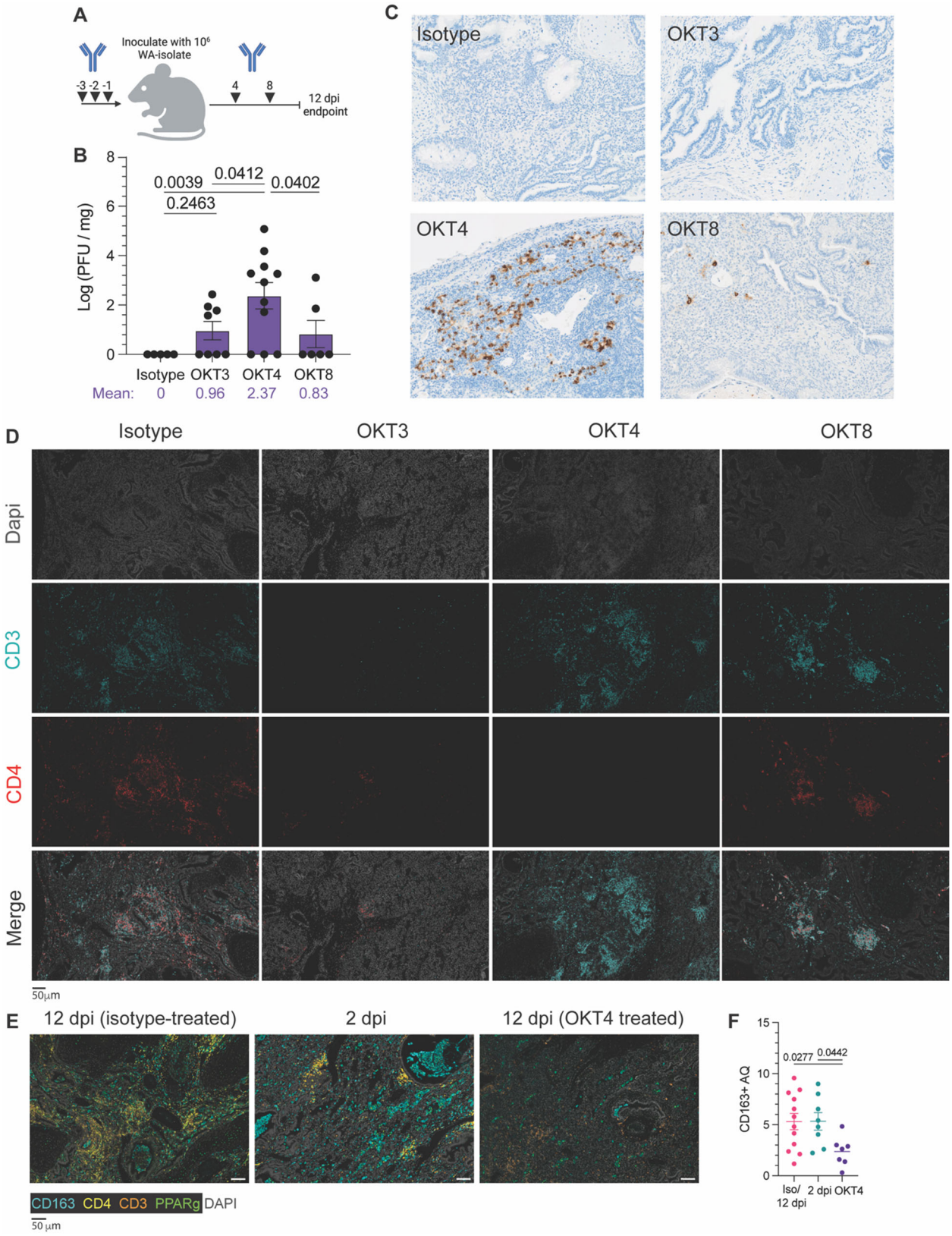
A
Inoculate with 10⁶ WA-isolate
-3 -2 -1
4
8
12 dpi endpoint
B
Log (PFU / mg)
0.0039
0.0412
0.0402
0.2463
Isotype
OKT3
OKT4
OKT8
Mean: 0 0.96 2.37 0.83
C
Isotype
OKT3
OKT4
OKT8
D
Isotype
OKT3
OKT4
OKT8
Dapi
CD3
CD4
Merge
50µm
E
12 dpi (isotype-treated)
2 dpi
12 dpi (OKT4 treated)
CD163 CD4 CD3 PPARg DAPI
50 µm
F
CD163+ AQ
0.0277
0.0442
Iso/ 12 dpi
2 dpi
OKT4

1014

1015 **Figure 9. Systemic depletion of CD4+ cells results in persistent infection of fLX. (A)** BLT-L
1016 mice were administered 200 μg of anti-CD3e (OKT3), anti-CD4 (OKT4), anti-CD8 (OKT8) or
1017 IgG2a isotype. **(B)** Viral titer (log(PFU/mg)) in fLX extracted from BLT-L mice treated with isotype,
1018 OKT3, OKT4, or OKT8 antibody at 12 dpi. **(C)** Immunohistochemistry for SARS-CoV-2 N protein
1019 on fLX of depleted or non-depleted BLT-L mice at 12 dpi. **(D)** Multiplex immunohistochemistry on
1020 fLX of depleted or non-depleted BLT-L mice at 12 dpi. Dapi = gray, CD3 = teal, CD4 = red. Scale
1021 bar = 50 μm. **(E-F)** Multiplex fluorescent immunohistochemistry (E) and CD163+ area
1022 quantification (AQ) (F) of fLX that resolved infection (12 dpi, isotype treated), or eliciting acute (2
1023 dpi) or persistent infection (12 dpi, OKT4 treated). CD163: teal, CD4: yellow, CD3: orange,
1024 PPARγ: green, Dapi: gray. Scale bar = 50 μM.
1025

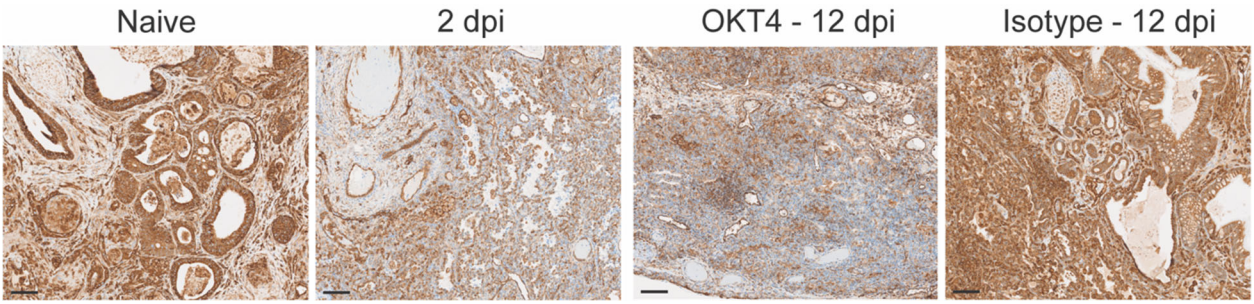


1026
1027 **Figure 10.** MHC-I staining of fLX tissue sections (anti-MHC class I (EMR8-5) CST 88274)
1028 extracted from naïve mice, OKT4-treated mice (12 dpi), or from infected fLX at 2 and 12 dpi. Scale
1029 bar = 100 μM
1030
1031
1032
1033
1034
1035

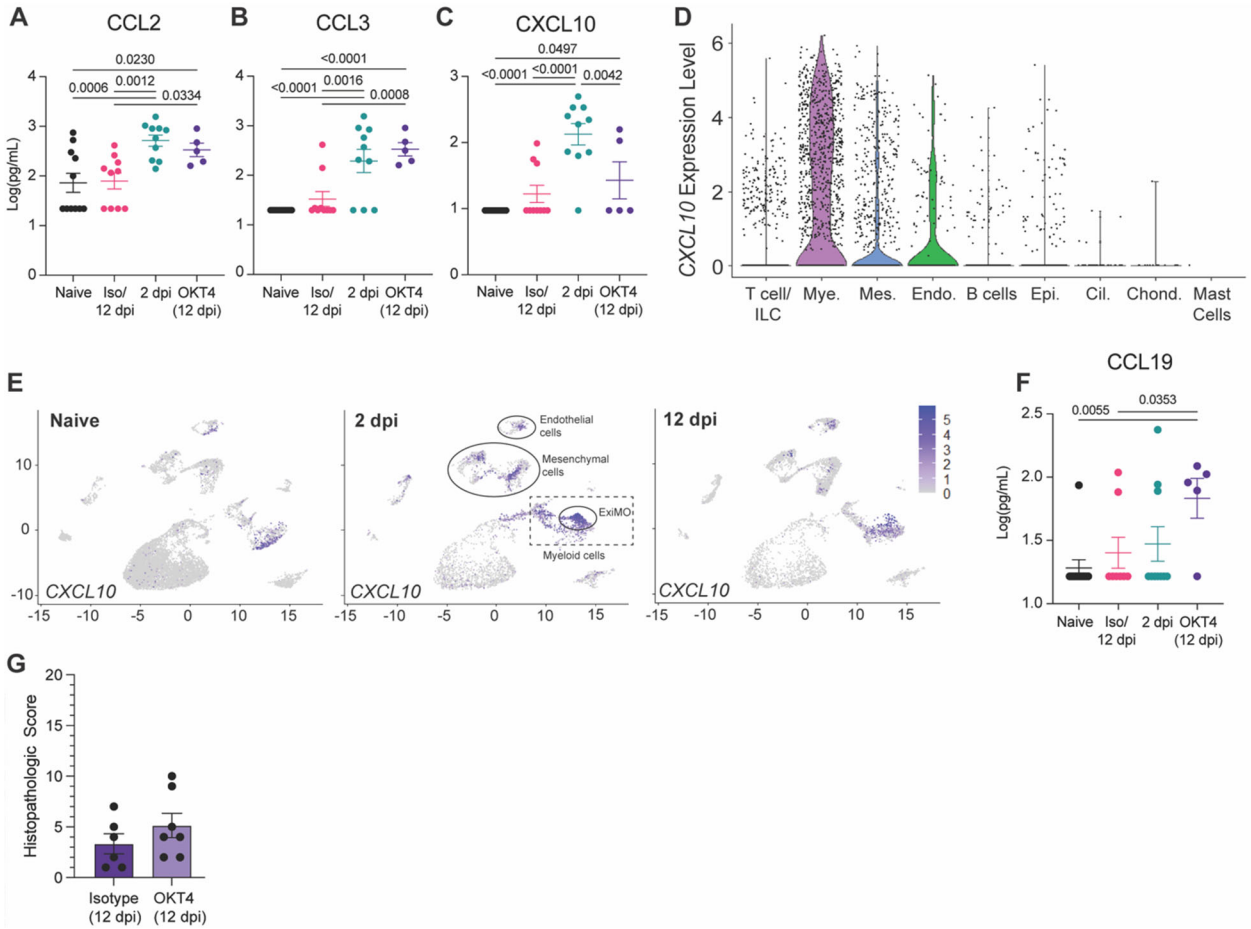


**Figure 11. CD4+ cell depletion results in signatures of chronic infection. (A-C)** Cytokine quantification (**A**: CCL2, **B**: CCL3, **C**: CXCL10) in the serum of naïve, infected (2 dpi and 12 dpi isotype-treated or not) and OKT4-treated BLT-L mice (12 dpi). **(D)** Violin plot showing expression level of *CXCL10* per cell and within each human lineage. **(E)** UMAP plot showing *CXCL10* expression within all human lineages in naive fLX and at 2- and 12 dpi. Locations of the mesenchymal, endothelial, myeloid and ExiMO clusters at 2 dpi are indicated. **(F)** Quantification of CCL19 in the serum of naïve, infected (2 dpi and 12 dpi isotype-treated or not) and OKT4-treated BLT-L mice (12 dpi). **(G)** Histopathological scoring of fLX extracted from isotype and OKT4-depleted BLT-L mice (12 dpi). Error bars indicate mean ± Standard error of the mean. One-*way ANOVA, t-test. p-values are indicated on graphs.*

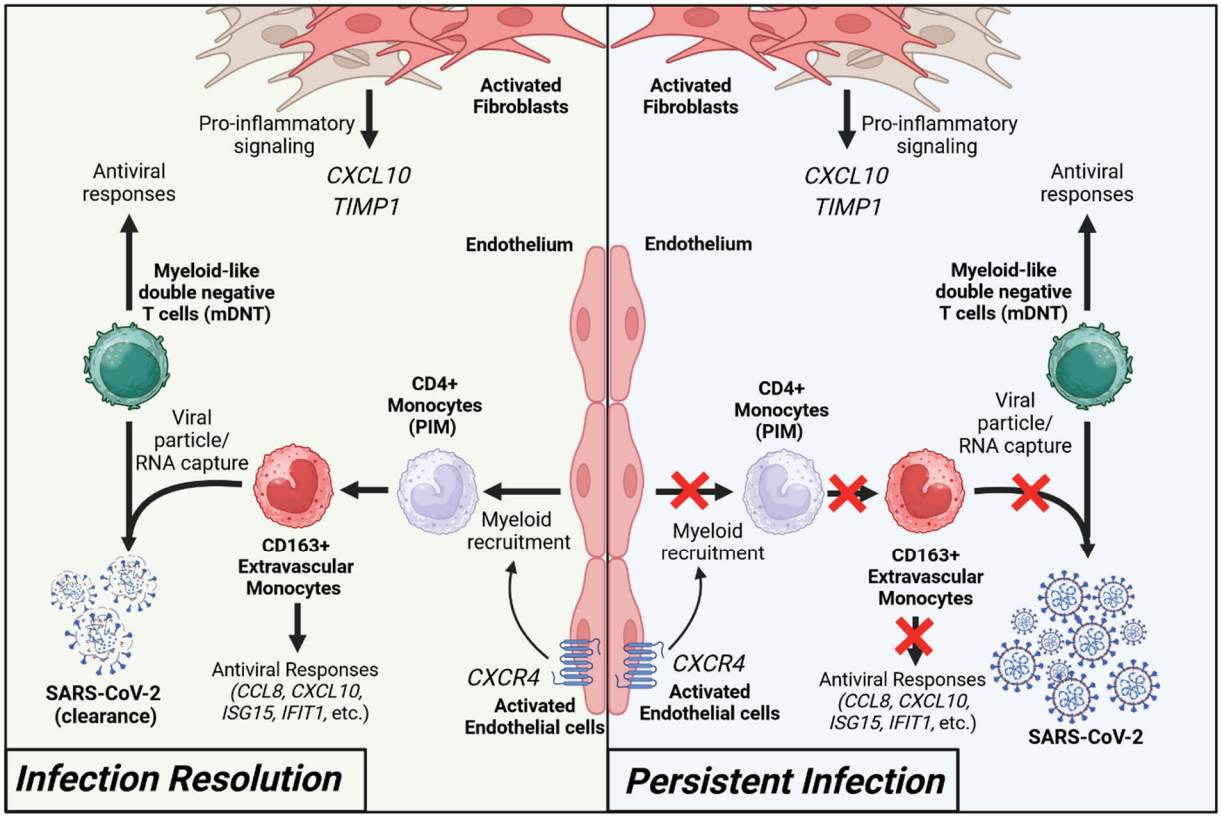


**Figure 12. Immune signatures of SARS-CoV-2 infection resolution in human lung tissues.** During effective viral resolution and tissue repair (left panel), myeloid cells are recruited to the site of infection and differentiates into CD163+ inflammatory monocytes (iMO). iMO produce antiviral and inflammatory signals and capture viral RNA/particles. Additionally, myeloid-like double negative T cells (mDNT), act to enhance the capture of viral RNA/particles and antiviral responses. In parallel, activated endothelial cells and fibroblasts contribute to the recruitment of myeloid cells and inflammatory response, respectively. Collectively, these events lead to viral clearance and infection resolution. In the context of persistent infection (left panel), absence of effective CD4+ monocyte recruitment prevents infection resolution.